Report 32: Age groups that sustain resurging COVID-19 epidemics in the United States v2 - SUPPLEMENT

Mélodie Monod*, Alexandra Blenkinsop*, Xiaoyue Xi*, Daniel Hebert*, Sivan Bershan*, Simon Tietze*, Marc Baguelin, Valerie C Bradley, Yu Chen, Helen Coupland, Sarah Filippi, Jonathan Ish-Horowicz, Martin McManus, Thomas Mellan, Axel Gandy, Michael Hutchinson, H Juliette T Unwin, Michaela A C Vollmer, Sabine L van Elsland, Sebastian Weber, Harrison Zhu, Anne Bezancon, Neil M Ferguson, Swapnil Mishra, Seth Flaxman[1], Samir Bhatt[1], and Oliver Ratmann[1,*], on behalf of the Imperial College COVID-19 Re-sponse Team

Department of Mathematics, Imperial College London
Foursquare Inc.
Emodo Inc.
Department of Infectious Disease Epidemiology, Imperial College London
WHO Collaborating Centre for Infectious Disease Modelling
MRC Centre for Global Infectious Disease Analytics
Abdul Latif Jameel Institute for Disease and Emergency Analytics, Imperial College London
Novartis Pharma AG, Basel, Switzerland
Department of Statistics, University of Oxford

*Contributed equally.
[1]Corresponding authors: Oliver Ratmann, oliver.ratmann@imperial.ac.uk;
Samir Bhatt, s.bhatt@imperial.ac.uk; Seth Flaxman, s.flaxman@imperial.ac.uk

SUGGESTED CITATION
M Monod, A Blenkinsop, X Xi *et al.* Report 32: Age groups that sustain resurging COVID-19 epidemics in the United States - VERSION 2 SUPPLEMENT. Imperial College London (07-01-2021), doi: https://doi.org/10.25561/82551.

Contents

DOI: https://doi.org/10.25561/82551

S1 National mobility indicators during the pandemic

S1.1 Age-specific U.S. foot traffic

To characterise changes in human contact patterns during the pandemic, Foursquare Labs Inc. provided longitudinal U.S. foot traffic data across the 50 U.S. states, the District of Columbia, and New York City [1]. The data are based on Foursquare's US first-party panel that includes millions of opt-in, always-on active users. Visits are derived via Foursquare's core location technology, Pilgrim [2], which leverages a variety of mobile device signals to pinpoint the time, duration, and location of panelists' visits to locations such as shops, malls, restaurants, concert venues, theaters, parks, beaches, or universities. From operated and partner apps, Foursquare Labs Inc. collect a variety of device signals against opted-in users. These include intermittent device GPS coordinate pings, WiFi signals, cell signal strength, device model, and operating system version. Additionally, a smaller set of labeled explicit check-ins are captured from a portion of the user panel. Check-ins are explicit confirmations that a user was at a given venue at a given point of time. One example source of this is Foursquare's Swarm app, where users can "check in" to venues to keep a log of where their mobility history. These check-ins then serve as training labels for a non-linear model that is used to predict visits among users with unlabeled visits in terms of probabilities as to which venue users ultimately visited. For research and insights use cases, the probabilities are processed further, projected and aggregated by state / metropolitan area, day, and age cohort. This projection accounts for changes in the number of individuals in the panel and the representativeness of panelists according to their home state or metropolitan area, age band, and gender relative to latest US Census data.

Daily projected visit volumes were available at state / metropolitan area-level from February 1, 2020 to October 29, 2020 for individuals for 6 age groups

$$\tilde{a} \in \tilde{\mathcal{A}} = \Big\{[18-24], [25-34], [35-44], [45-54], [55-64], [65+]\Big\}. \tag{S1}$$

Daily projected visit volumes were standardised to projected per capita visits $V_{m,t,\tilde{a}}$ of individuals in state / metropolitan area m and age band $\tilde{a}$ on day t by dividing the visit volumes with the number of individuals in state / metropolitan area m and age band $\tilde{a}$. Per capita visits appeared low for the first two days of the time series, and were excluded. Data updates were obtained from May 26 onwards.

Fig. S17 illustrates the pre-processed time series of projected per capita visits $V_{m,t,\tilde{a}}$. Individuals in New York City, New York, and Hawai were projected to have considerably more per capita visits than other states and metropolitan areas. Across states and metropolitan areas, projected per capita visits were highest for individuals aged $35-44$ years, both before and after stay at home orders were issued. Individuals aged 65 or older had lowest projected per capita visits across all states and metropolitan areas.

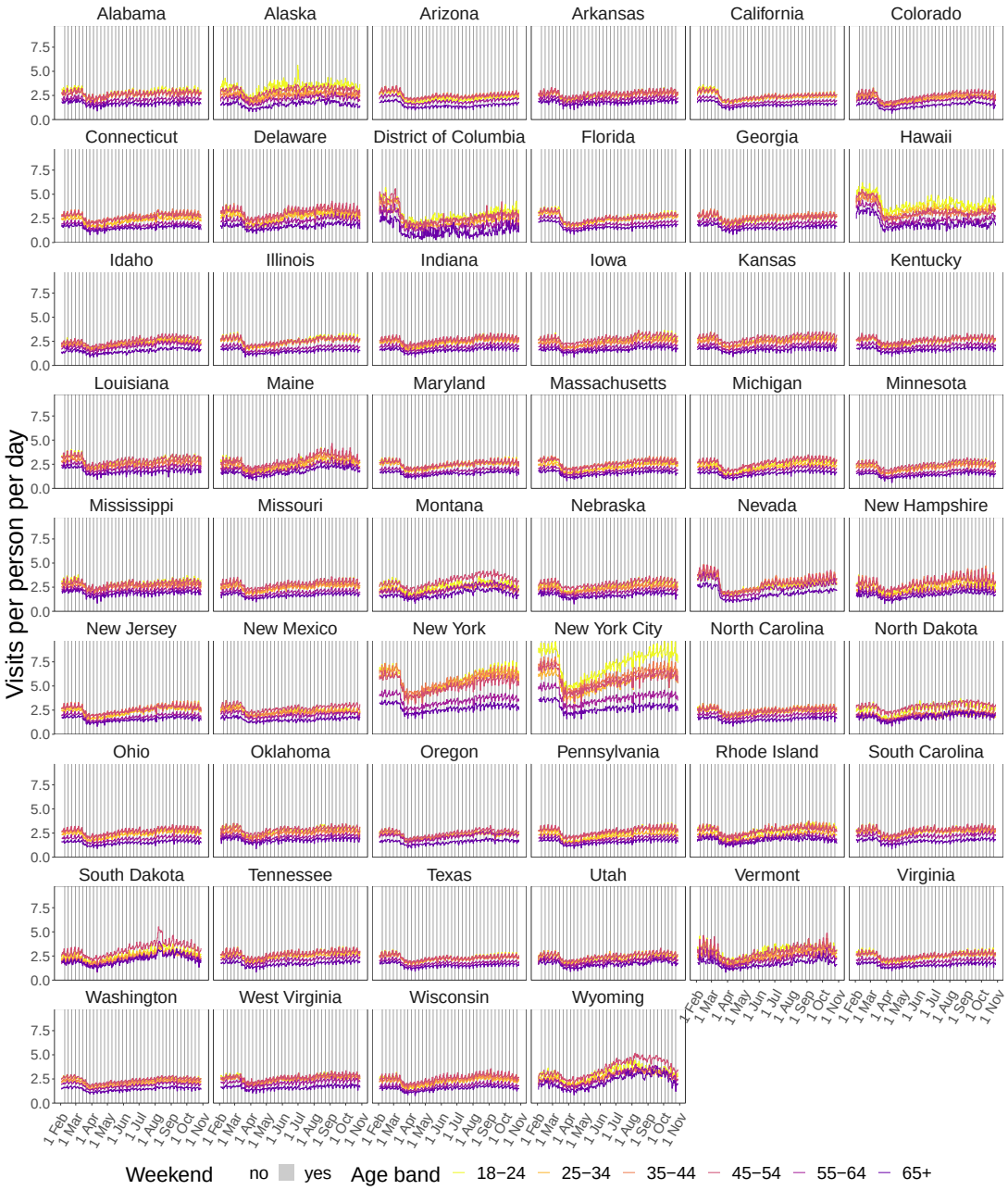

Figure S17: Projected per person foot traffic per day for the 50 US states, District of Columbia and New York City. Data were obtained using Foursquare's location technology Pilgrim that pinpoints the time, duration, and location of panelist's visits. Projected per capita visits standardised visit volumes by the population size in each location and age group.

S1.2 Age-specific U.S. mobility trends

Age-specific mobility trends were derived from the U.S. foot traffic data described in Section S1.1. Our aim was to quantify changes in U.S. foot traffic during the pandemic relative to a baseline period for individuals in the 5-year age bands (S21) in each of the U.S. states, the District of Columbia, and New York City. The baseline period was defined from February 3 to February 9, 2020, which corresponded to the first week of the time series of projected per capita visits. We first calculated average projected per capita visits during the baseline week,

$$V_{m,\tilde{a}}^{\text{base}} = \sum_{t \in \{\text{Feb 3} - \text{Feb 9}\}} V_{m,t,\tilde{a}} \tag{S2}$$

and then derived the mobility trends

$$X_{m,t,\tilde{a}} = V_{m,t,\tilde{a}} / V_{m,\tilde{a}}^{\text{base}} \tag{S3}$$

for each state / metropolitan area m and the age bands $\tilde{a}$ available through the U.S. foot traffic data.

S1.3 Quantitative Analysis

To characterise different effects during the initial phase of the pandemic, the time when stay at home orders were introduced, and later time periods, we derived two particular time points for each state or metropolitan area. The first time point characterises the start of substantial declines in mobility across all age groups, and the second time point characterises the time after which mobility trends begin to rebound. To determine the two time points we calculated the 15-days central moving average of projected per capita visits in each location (state or metropolitan area) m,

$$X_{m,t}^{\text{m-avg}} = \frac{1}{30+1} \frac{1}{\tilde{A}} \sum_{s=-15}^{15} \sum_{\tilde{a}} X_{m,t+s,\tilde{a}}, \tag{S4}$$

where $\tilde{A}$ is the number of age groups in the mobility data specified in (S1), such that $\tilde{A} = 6$. The first time point, which we refer to as the dip date, was determined as the first day when the 15-days moving-average had fallen by over 10% compared to the one two weeks prior,

$$t_m^{\text{dip}} = \min\{t : X_{m,t}^{\text{m-avg}} / X_{m,t-14}^{\text{m-avg}} < 0.9\}. \tag{S5}$$

The second time point, which we refer to as the rebound date, was determined as the day with the smallest 15-days moving-average,

$$t_m^{\text{rebound}} = \text{argmin}_{t > t_m^{\text{dip}}} X_{m,t}^{\text{m-avg}}, \tag{S6}$$

where $t_m^{\text{dip}} < t_m^{\text{rebound}}, \forall m$. Using different time intervals in the central moving average calculations did not alter the value of change points substantially (not shown). Figure S1 shows the mobility trends (S3) for every U.S. state, the District of Columbia, and New York City, along with the dip and rebound dates.

We then assessed differences in the weekly, age-specific mobility trends when compared to the baseline week in early February. Gamma regression models with log link, and location and age category interaction terms were fitted to the selected daily mobility trends. Negative regression coefficients with a two-sided p-value below 0.05 were interpreted as age groups showing statistically significantly lower mobility compared to the baseline week. Similarly, positive regression coefficients with a two-sided p-value below 0.05 were interpreted as age groups showing statistically significantly higher mobility compared to the baseline week, and regression coefficients with a two-sided p-value above 0.05 were interpreted as age groups showing mobility trends that were not significantly different compared to the baseline week. Fig. S18 summarises the results. Overall, relative to the baseline week, mobility trends started to decline significantly in mid March, were not significantly lower than baseline levels for the first states in early to mid May, and not significantly lower than baseline levels for most states by early August.

Next, we compared the relative mobility trends between age groups over time, using the 35-44 age group for relative comparisons. Gamma regression models were fitted to the trend data similarly as described above. Fig. S19 summarises the results. Overall, individuals aged 18-24 had significantly lower mobility trends when compared to individuals aged 35-44 across most states in the early phase of the pandemic, between mid March and early June. No other age group showed similarly strong relative declines in mobility. However these relative differences weakened over time and since mid June, individuals aged 18-24 tended to have similar mobility trends as individuals aged 35-44. The only notable exception are younger individuals aged 18-24 (and also those aged 25-34) in Hawaii, who tended to have significantly higher mobility trends than individuals aged 35-44 throughout the entire observation period. Overall, individuals aged $65+$ also had significantly lower mobility trends than those aged 35-44, although less consistently across states when compared to young individuals. In conclusion, the Foursquare data suggest that, except for Hawaii, individuals aged 18-34 have lower or similar, but not significantly higher mobility when compared to individuals aged 35-44. In addition, individuals aged 18-24 showed significancly lower mobility trends when compared to individuals aged 35-44 between mid March and early June in most states.

S1.4 Comparison of Foursquare mobility trend data set to an independent U.S. mobility trend data set

To substantiate the trends observed in the national Foursquare data set, we evaluated an independent data set of age-stratified mobility indicators that was provided by Emodo. The Emodo data set quantifies the proportion of individuals with at least one observed ping outside the user's home location, out of a panel of individuals whose GPS enabled devices emitted at least one ping on the corresponding day. The observed, age-specific, daily mobility indicators within the panel were projected to location-level mobility indicators. The projection accounts for changes in the number of individuals in the panel, and the representativeness of panel members in their home area, age band, and gender relative to the latest

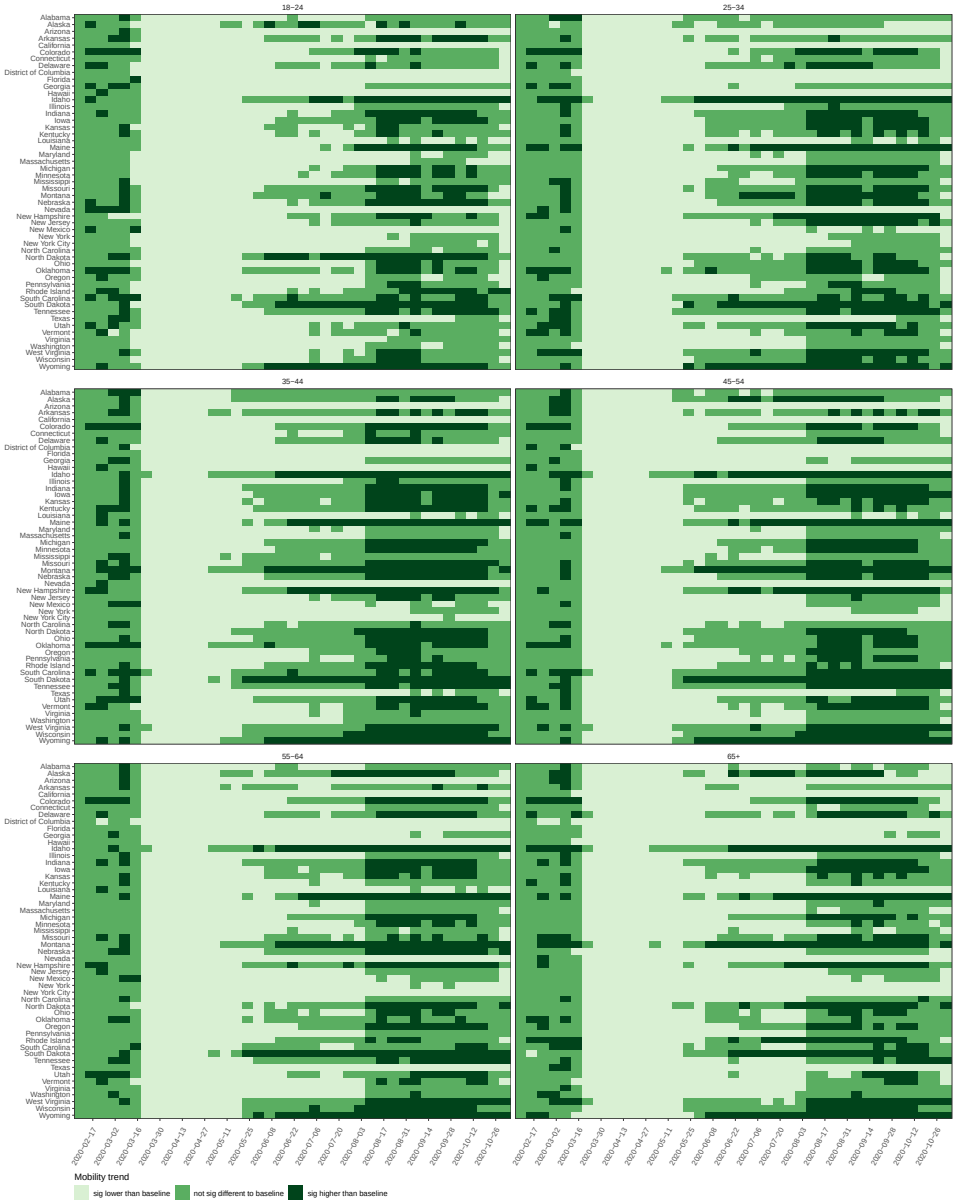

Figure S18: Analysis of mobility trends relative to the baseline week. Gamma regression models with log link were fitted to the daily trends. For each calendar week, mobility trends were categorised as statistically significantly lower when compared to the baseline week, not significantly different, and statistically higher.

Figure S19: Analysis of mobility trends relative to trends among individuals aged $35-44$. Gamma regression models with log link were fitted to the daily trends. For each calendar week and each age group, mobility trends were categorised as statistically significantly lower when compared to the trends among individuals aged $35-44$ in the same week, not significantly different, and statistically higher.

U.S. Census.

Daily projected mobility indicators $\breve{V}_{m,t,\breve{a}}$ were available at state / metropolitan area-level m from Feb 01 to Jul 26 for individuals between the age groups

$$\breve{a} \in \breve{\mathcal{A}} = \Big\{[18-24], [25-34], [35-44], [45-54], [55+]\Big\}. \tag{S7}$$

To compare the data against the age-specific Foursquare mobility trends (S3), we derived mobility trends similarly as for the Foursquare data. We first calculated average mobility trends during the baseline period,

$$\breve{V}^{\text{base}}_{m,\breve{a}} = \sum_{t \in \{\text{Feb 19}-\text{Mar 03}\}} \breve{V}_{m,t,\breve{a}} \tag{S8}$$

and then derived the mobility trends

$$\breve{X}_{m,t,\breve{a}} = \breve{V}_{m,t,\breve{a}} / \breve{V}^{\text{base}}_{m,\breve{a}} \tag{S9}$$

for each location (states or metropolitan area) m and the age bands $\breve{a}$.

Initial analysis indicated that the mobility trends (S9) were noisy for some locations. For this reason, analysis was limited to location with an average of $20,000$ distinct panelists per day per age band, and the baseline period in (S8) was defined over 14 days. In total, data from 11 locations were used. Fig. S20 compares the age-specific mobility trends derived from the Foursquare data to those derived from the Emodo data set. Overall, the trends observed in both data sets were very similar until mid July. Since mid July, the Emodo data suggest that mobility trends plateaued below baseline levels, whereas the Foursquare data suggest that mobility continued to increase in all age groups.

The primary aim of this analysis was to assess whether the Emodo data support the above observation that individuals aged $18-24$ and $25-34$ had mobility trends that are not significantly higher than those seen for older individuals. We repeated the analyses presented in Section S1.2, with the last observation week set to the last complete week of observations in both data sets (September 20, 2020). Fig. S21 summarises the results. The Emodo data substantiate that individuals aged 18-24 and $25-34$ had lower or similar mobility levels than individuals aged 34-45, and not higher mobility levels than individuals aged 34-45.

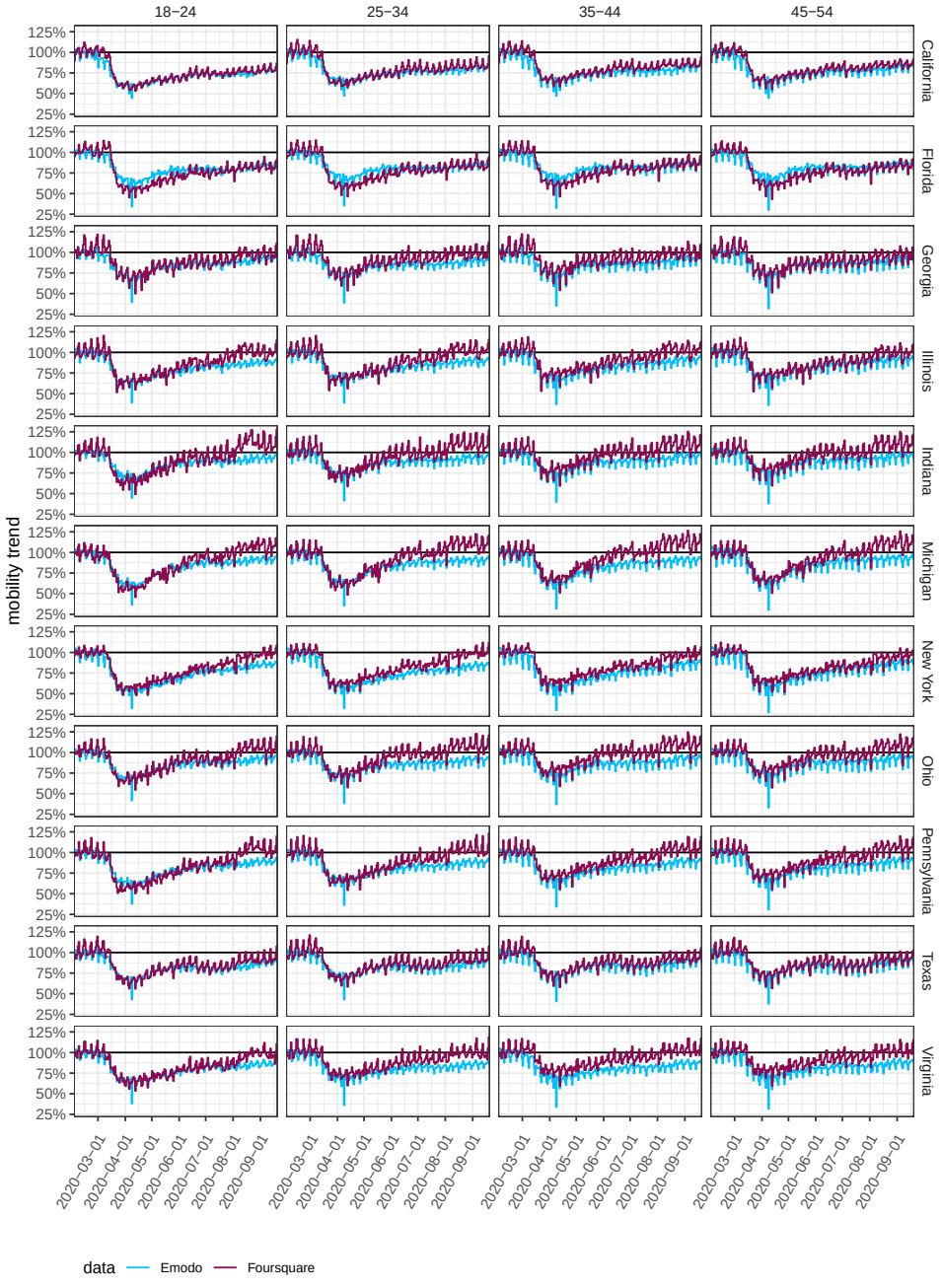

Figure S20: Comparison of mobility trends derived with Foursquare's location technology and Emodo's mobility data. The comparison was restricted to identical age bands in the two data sets, a common range of observation days, and states and metropolitan areas with an average of at least $20,000$ panelists per day.

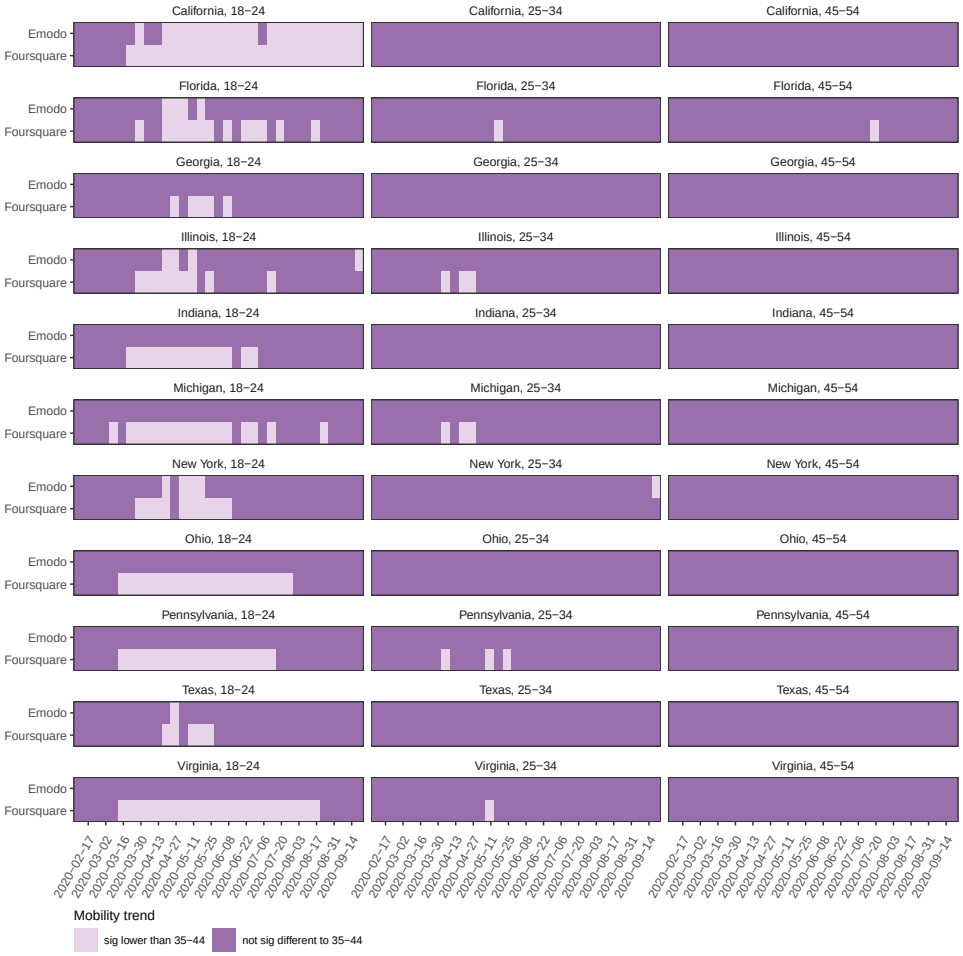

Figure S21: Comparison of mobility trends in the Foursquare and Emodo data sets relative to the 35-44 reference age group. For each calendar week and each age group, mobility trends were categorised as statistically significantly lower when compared to the trends among individuals aged $35 - 44$ in the same week, not significantly different, and statistically higher. Results based on the Emodo data set are plotted above those for the Foursquare data set. The comparison was restricted to identical age bands in the two data sets, a common range of observation days, and states and metropolitan areas with an average of at least $20,000$ panelists per day.

S2 Age-specific COVID-19 attributable mortality data

S2.1 Source of the unstratified and age-specific COVID-19 deaths data

Daily COVID-19 death counts from February 01, 2020 until October 30, 2020 regardless of age were obtained from John Hopkins University (JHU) for all U.S. states and the District of Columbia [3], except New York State. For New York City, daily COVID-19 deaths counts were obtained from the GitHub Repository [4]. The overall death counts were used for statistical inference prior to when age-specific death counts were reported for each location (state or metropolitan areas).

Age-specific COVID-19 cumulative death counts were retrieved for 43 US states, the District of Columbia and New York City from city or state Department of Health (DoH) websites, data repositories or via data requests to DoH. Table S8 lists our data sources for each location, the date since when age-specific mortality data used in this study was recorded, and the frequency of data updates.

S2.2 Data collection and processing of the age-specific COVID-19 deaths counts

The recorded death counts were processed to create a time series of daily deaths for every location. Some dates had missing data, typically either because no updates were reported, because the webpage failed or because the URL of the website had mutated. Missing daily death counts were imputed, assuming a constant increase in daily deaths between two days with data. Some updates displayed a decreasing cumulative death from one day. To ensure that the time series was monotonically increasing, we back adjust with the most recent count assumed to be the correct cumulative count. Finally, certain age bands declared by the Department of Health could not be directly associated with the age bands used in the analysis, defined in (S21). In this case, the boundaries of these problematic age bands were modified to reflect the closest age band from the analysis. Fig. S7 illustrates the age-specific COVID-19 mortality data that were retrieved. To assess the completeness of the age-specific death data, we compared the time evolution of the sum of the age-specific deaths that we retrieved to the time evolution of the overall number of COVID-19 deaths reported by JHU [3] and the New York City Github Repository [4]. Fig. S22 confirms that the sum of the age-specific data that we retrieved closely matched the overall death data.

S2.3 Share of deaths and cases by common age strata across locations

For an initial analysis of the time evolution of death counts across locations, the data from different age stratifications were used to predict death counts in the common age bands $\mathcal{A}$ defined in (S21) across all locations using a latent Dirichlet-multinomial model. Denote by $\mathcal{B}_{mt}$ the age bands specified in location m in month t by the DoH. To ensure that deaths by all age bands are mapped correctly, the latent Dirichlet-multinomial model uses internally the 1-year stratification

$$\check{\mathcal{A}} = \{0, 1, \ldots, 104, 105\}. \tag{S10}$$

We denote the COVID-19 attributable deaths occurring in location m in calendar month t by $\mathbf{y}_{\check{\mathcal{A}},mt} = [y_{mt\check{a}}]_{\check{a}\in\check{\mathcal{A}}}$. In other words, $y_{mt\check{a}}$ are the sum of the daily new COVID-19 attributable deaths that occurred in location m within calendar month t among individuals in the 1-year age bands $\check{a}$. The monthly deaths $\mathbf{y}_{\check{\mathcal{A}},mt}$ are not observed, and assumed to follow a distribution specified by a combination of several base functions that depend only on age. To simplify notation, we suppress the location and time indices in the following, with all variables and parameters being specific to one location and one month. We adopted the parametric model

$$\mathbf{y}_{\check{\mathcal{A}}} \sim \text{Dirichlet-multinomial}(N, \kappa \times \boldsymbol{\psi}_{\check{\mathcal{A}}}), \tag{S11a}$$

$$\boldsymbol{\psi}_{\check{\mathcal{A}}} = \text{softmax}(\boldsymbol{\vartheta}_{\check{\mathcal{A}}}), \tag{S11b}$$

$$\vartheta_{\check{\mathcal{A}},\check{a}} = \omega_1 + \omega_2\, \check{a} + \omega_3\, \check{a}^2 + \omega_4 \log(\check{a}), \quad \text{for all } \check{a} \in \check{\mathcal{A}}, \tag{S11c}$$

where $N = \sum_{\check{a}} y_{\check{a}}$ and the softmax function is

$$\text{softmax}(\boldsymbol{z})_{\check{a}} = \frac{\exp(z_{\check{a}})}{\sum_{k\in\check{\mathcal{A}}} \exp(z_k)}. \tag{S12}$$

Because of the self-normalising property of the softmax function, the vector $\boldsymbol{\psi}$ can be interpreted as the unknown, expected proportions of death counts that fall into the fine-resolution age bands $\check{a} \in \check{\mathcal{A}}$. Thus, the above model describes the expected proportions as a combination of constant, linear, square and logarithmic functions on the untransformed scale. The model is straightforward to fit to the observed death counts in the reporting strata $\mathcal{B}$ by the aggregation property of the Dirichlet-multinomial distribution. Denote the reported deaths by $\mathbf{y}_{\mathcal{B}} = [y_b]_{b\in\mathcal{B}}$. Then, the likelihood of the fine-resolution model is

$$\mathbf{y}_{\mathcal{B}} \sim \text{Dirichlet-multinomial}(N, \kappa \times \boldsymbol{\psi}_{\mathcal{B}}) \tag{S13a}$$

$$\boldsymbol{\psi}_{\mathcal{B}} = \text{softmax}(\boldsymbol{\vartheta}_{\mathcal{B}}) \tag{S13b}$$

$$\vartheta_{\mathcal{B},b} = \sum_{\check{a}\in b} \vartheta_{\check{\mathcal{A}},\check{a}} \quad \text{for all } b \in \mathcal{B}. \tag{S13c}$$

The Dirichlet-multinomial allows for overdispersion in the fine-resolution death counts. A priori, we sought to allocate highest probability mass to the sub-model without overdispersion, which we obtained with the re-parameterisation

$$1 + \nu = \frac{N + \kappa}{1 + \kappa}, \tag{S14}$$

and adopting the prior densities

$$\omega_i \sim \mathcal{N}(0, 1), \quad i = 1, \ldots, 4, \tag{S15a}$$

$$\nu \sim \text{Exponential}(1). \tag{S15b}$$

The fine resolution model was fitted with Stan version 2.23, using 3 Hamiltonian Monte Carlo Markov Chains of 10,000 iterations and 1,000 warmup iterations. All chains mixed well, had good convergence

diagnostics, no divergent transitions, and the effective sample size for all parameters was above 500 in all analyses.

The proportion of deaths in the common age stratification $\mathcal{A}$ and the corresponding death counts were predicted from the fitted fine-resolution model. Specifically, denote the predicted proportions of deaths and deaths counts respectively by $\boldsymbol{\varphi}^\star_a$, $\boldsymbol{d}^\star_a$. Then, we sampled $\boldsymbol{\varphi}^\star_a$, $\boldsymbol{d}^\star_a$ according to their posterior predictive distributions. For samples $(\boldsymbol{\psi}, \kappa)|\mathbf{y}_\mathcal{B}$ from the joint posterior distribution of the fine-resolution model, we used again the aggregation property of the Dirichlet-multinomial distribution,

$$\boldsymbol{\psi}_\mathcal{A}|\mathbf{y}_\mathcal{B} = \text{softmax}(\boldsymbol{\vartheta}_\mathcal{A}) \tag{S16}$$

$$\vartheta_{\mathcal{A},c}|\mathbf{y}_\mathcal{B} = \sum_{\check{a}\in a} \vartheta_{\check{\mathcal{A}},\check{a}}|\mathbf{y}_\mathcal{B} \quad \text{for all } d \in \mathcal{C}, \tag{S17}$$

and then predicted

$$\boldsymbol{\varphi}^\star_\mathcal{A}|\mathbf{y}_\mathcal{B} \sim \text{Dirichlet}(\kappa \times \boldsymbol{\psi}_\mathcal{A}|\mathbf{y}_\mathcal{B}), \tag{S18}$$

$$\boldsymbol{d}^\star_a|\mathbf{y}_\mathcal{B} \sim \text{Multinomial}(N, \boldsymbol{\varphi}^\star_\mathcal{A}|\mathbf{y}_\mathcal{B}). \tag{S19}$$

We back-calculated the monthly number of cases, $\boldsymbol{c}^\star_a$, by dividing the estimated number of deaths by the infection fatality rate in the corresponding age group,

$$\boldsymbol{c}^\star_a|\boldsymbol{d}^\star_a = \boldsymbol{d}^\star_a \,/\, \pi_a, \tag{S20}$$

where π_a is the infection fatality rate in age group a estimated in the meta-analysis by Levin and colleagues [5].

Figure S11 shows the monthly share of deaths for all age group and Figure S12 shows the monthly share of cases over time among individuals aged $20-49$. To evaluate if any the age-specific share changed significantly over time, we computed for every month the share's difference relative to the first month with at least 30 cumulative deaths. On Figure S11, we added a star (*) next to the name of locations for which there was a significant shift in the share of deaths among individuals age $80+$. In Figure S12, we added a star (*) next to the name of locations for which there was a significant shift in the share of cases among individuals age $20-49$.

Table S8: Age-specific Mortality Data source, date of first availability and update frequency by location (state and metropolitan area). The data are available in the GitHub repository [6].

Location	Date record start	Frequency of updates	Source
Alabama	May 03, 2020	Daily	[7]
Alaska	June 09, 2020	Daily	[8]
Arizona	May 13, 2020	Daily	[9]
Arkansas	-	-	-
California	May 13, 2020	Daily	[10]
Colorado	March 23, 2020	Daily	[11]
Connecticut	April 05, 2020	Daily	[12]
Delaware	May 12, 2020	Daily	[13]
District of Columbia	April 13, 2020	Daily	[14]
Florida	March 27, 2020	Daily	[15]
Georgia	May 09, 2020	Daily	[16]
Hawaii	September 18, 2020	Weekly	[17]
Idaho	June 16, 2020	Daily	[18]
Illinois	May 14, 2020	Daily	[19]
Indiana	May 13, 2020	Daily	[20]
Iowa	May 13, 2020	Daily	[21]
Kansas	June 02, 2020	Mon, Wed and Fri.	[22]
Kentucky	May 13, 2020	Daily	[23]
Louisiana	May 12, 2020	Daily except Sat.	[24]
Maine	March 12, 2020	Daily	[25]
Maryland	May 14, 2020	Daily	[26]
Massachusetts	April 20, 2020	Daily	[27]
Michigan	March 21, 2020	Daily	[28], [29]
Minnesota	May 21, 2020	Weekly	[30]
Mississippi	September 30, 2020	Daily	[31]
Missouri	May 13, 2020	Daily	[32]
Montana	-	-	-
Nebraska	-	-	-
Nevada	June 07, 2020	Daily	[33]
New Hampshire	June 07, 2020	Daily	[34]
New Jersey	May 25, 2020	Daily	[35]
New Mexico	March 25, 2020	Daily	[36]
New York	-	-	-
New York City	July 01, 2020	Daily	[37], [4]
North Carolina	May 20, 2020	Daily	[38]
North Dakota	May 14, 2020	Daily	[39]
Ohio	-	-	-
Oklahoma	May 13, 2020	Daily	[40]
Oregon	June 05, 2020	Mon-Fri., sometimes Sat.	[41]
Pennsylvania	June 07, 2020	Daily	[42]
Rhode Island	June 01, 2020	Weekly	[43]
South Carolina	May 14, 2020	Tue and Fri.	[44]
South Dakota	-	-	-
Tennessee	April 09, 2020	Daily	[45]
Texas	July 28, 2020	Daily	[46]
Utah	June 17, 2020	Daily	[47]
Vermont	June 16, 2020	Daily	[48]
Virginia	April 21, 2020	Daily	[49]
Washington	June 08, 2020	Daily	[50]
West Virginia	-	-	-
Wisconsin	March 15, 2020	Daily	[51]
Wyoming	September 22, 2020	Daily	[52]

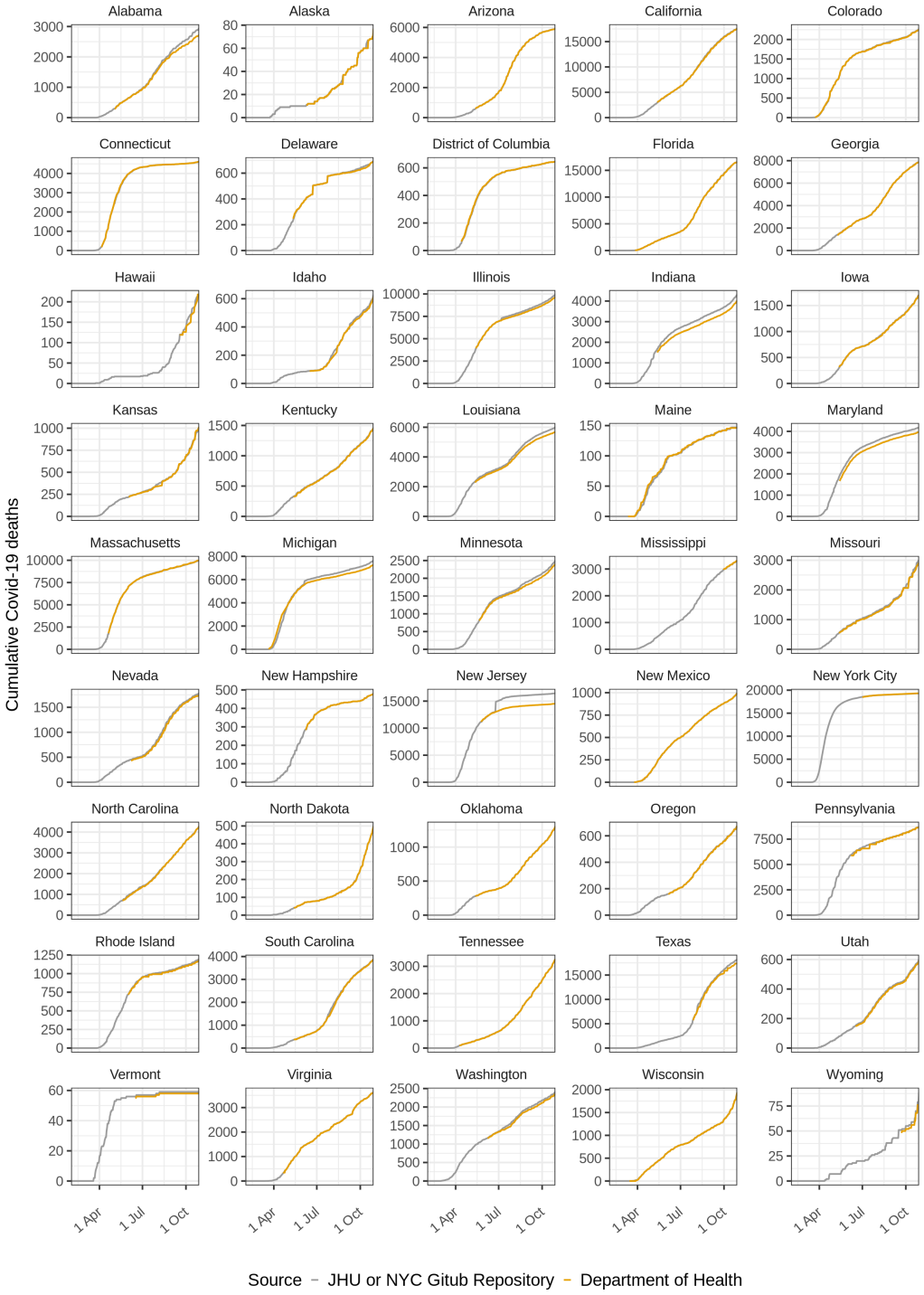

Figure S22: Comparison of the Covid-19 overall death between the Department of Health death by age data with the overall death from JHU [3], and the New York City Github repository (for NYC) [4].

S3 Bayesian semi-mechanistic SARS-CoV-2 infection model

Figure S23 summarises the main components of the age-specific contact and infection model. Section S3.1 describes the infection component of the model, and Section S3.2 describes the contact component of the model. Section S3.3 describes how the model is fitted against age-specific mortality data. Section S3.4 specifies input parameters and prior distributions. Table S9 gives an overview of the model parameters and associated prior distributions. Section S3.6 describes the generated quantities of the contact and infection model. Finally, Section S3.5 provides details on computational inference.

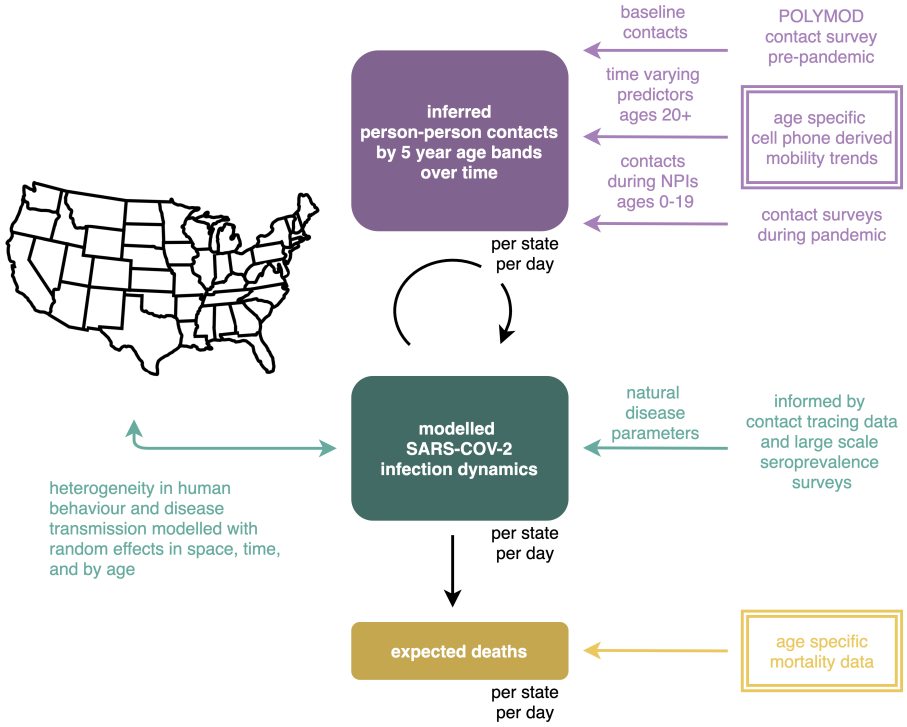

Figure S23: Overview of the age-specific contact and infection model.

Table S9: List of inputs and model parameters.

Name	Estimated	Prior	Notes	Section reference
Initial number of infections	yes	$\log c_{m,t,[20-54]} \sim \mathcal{N}(4.85, 0.4^2)$, $c_{m,t,a} = 0$, for $a \notin [20-54]$, where $t = 1, \ldots, 6$.	infections seeded among individuals aged 20-54 with log-normal prior with mean 138	Section S3.4.1
Infection parameters	yes	$\log R_{0,m} \sim \mathcal{N}(0.98, 0.2^2)$	Based on [53] with log-normal prior with mean, 2.5% and 97.5% quantiles: 2.7, 1.8, and 3.9.	Section S3.4.1
Susceptibility to infection	yes	$\log \rho^S_{[0-14]} \sim \mathcal{N}(-1.07, 0.22^2)$ $\log \rho^S_{[65+]} \sim \mathcal{N}(0.38, 0.16^2)$	Susceptibility was modelled relative to individuals aged 15-64, with lower susceptibility to infection among individuals aged 0-14, and higher susceptibility among individuals aged 65+. Based on [54]	Section S3.4.1
Discretized generation time distribution	no	-	Based on [55]	Section S3.4.1
Baseline age-specific contact matrix before mobility decreased	no	-	Predicted based on locations' age composition and population density for weekdays and weekends	Section S3.4.2
Schools closure age-specific contact matrix	no	-	Used for individuals aged $[0-19]$ during school closure periods Based on [54]	Section S3.4.2
Mobility trend predictors	no	-	Decomposed into 3 components to allow for varying effect sizes	Section S3.4.2
Regression coefficients to describe time-varying contact intensities before the rebound date.	yes	$\beta^{\text{eased}}_m \sim \mathcal{N}(\beta^{\text{eased}}, \sigma^2_{\text{eased}})$ $\beta^{\text{eased}} \sim \mathcal{N}(0, 1)$ $\sigma_{\text{eased}} \sim \text{Exp}(1.5)$	Location-specific random effects to quantify the effect of rapid decreases in mobility between the dip date and the rebound date. Effects are assumed to be constant across age groups.	Section S3.4.2
Regression coefficients to describe time-varying contact intensities after the rebound date.	yes	$\beta^{\text{upswing}}_{m,t,a} = (\beta^{\text{upswing-base}} + \beta^{\text{upswing-age}}_{m,a}) \times \beta^{\text{upswing-time}}_{m,t}$ $\beta^{\text{upswing-base}} \sim \mathcal{N}(0, 1)$ $\beta^{\text{upswing-time}}_{m,t} = \varepsilon_{m,\lfloor c(t)/2 \rfloor}$ $\varepsilon_{m,1} \sim \mathcal{N}_{[0,\infty)}(0, 0.025^2)$ $\varepsilon_{m,v} \sim \mathcal{N}_{[0,\infty)}(\varepsilon_{m,v-1}, \sigma^2_\varepsilon)$ for $v > 1$ $\log \sigma_\varepsilon \sim \mathcal{N}(-1.2, 0.2^2)$ $\beta^{\text{upswing-age}}_{m,[20-49]} \sim \text{Exp}(\beta^{\text{upswing-age}}_{m,[20-49]})$ $\beta^{\text{upswing-age}}_{m,[20-49]} \sim \text{Exp}(0.1)$	Random effects to capture unobserved behavioral factors after the rebound date. Effects vary over time and age for each location. Time-varying effects are modelled with bi-weekly AR(1) processes.	Section S3.4.2
Reduction in contact intensities from/to school children	yes	$\eta^{\text{children}} \sim \text{Uniform}(0.1, 1.0)$	Vague prior density.	Section S3.4.2
Reduction in contact intensities among school children	yes	$\log \gamma \sim \mathcal{N}(0, 0.35)$	Prior centered on null hypothesis of no additional effect.	Section S3.4.2
Location and age-specific infection fatality ratios	yes	$\pi_{m,a} = \pi_a \times \delta_{m,a}$ $\log \pi_a \sim \mathcal{N}(\mu_a, \sigma^2_a)$ $\log \delta_{m,[20-49]} \sim \text{Exp}(\delta^{\text{IFR}}_{[20-49]})$ $\log \delta_{m,[50-69]} \sim \text{Exp}(\delta^{\text{IFR}}_{[50-69]})$ $\log \delta_{m,[70+]} \sim \text{Exp}(\delta^{\text{IFR}}_{[70+]})$ $\delta^{\text{IFR}}_{[20-49]}, \delta^{\text{IFR}}_{[50-69]}, \delta^{\text{IFR}}_{[70+]} \sim \text{Exp}(0.1)$	The prior distribution on age-specific fatality ratios π_a is based on the meta-analysis of [5]. μ_a, σ_a are specified in Table S11. Location- and age-specific random effects allow for heterogeneity across locations.	Section S3.4.3
Infection-to-death distribution	no	-	As in [56]	Section S3.4.3
Upper bound on attack rate among school-aged children	no	-	Upper bound was derived by multiplying reported attack rates in school settings with $\xi = 6$ in the central analysis. Parameter choice was motivated assuming that 50% of infected children and teens are asymptomatic [57].	Section S3.4.3
Overdispersion parameter	yes	$\phi \sim \mathcal{N}_{[0,\infty)}(0, 5)$	As in [56]	Section S3.4.3

DOI: https://doi.org/10.25561/82551

In the model, SARS-CoV-2 spreads via person-to-person contacts. Person-to-person contacts are described at the population level with the expected number of contacts made by one individual, referred to as contact intensities. Contact intensities are age-specific. Contact intensities vary across locations (states and metropolitan areas) according to each location' age composition and population density, and change over time. Data from contact surveys before the pandemic are used to define baseline contact intensities. Data from age-specific, cell phone derived mobility trends are used to estimate changes in contact intensities during the epidemic in each location, among individuals aged $20+$. Contact intensities involving individuals aged 0-19 are defined based on contact surveys conducted during the pandemic. Infection dynamics in each location are modelled through age-specific, discrete-time renewal equations over time-varying contact intensities. Natural disease parameters such as age-specific susceptibility to infection, the generation time distribution, and symptom onset and onset to death distributions are informed by epidemiologic analyses of contact tracing data. Age-specific infection fatality ratio estimates are informed by large-scale sero-prevalance surveys. Disease heterogeneity is modelled with random effects in space and time on contact intensities and disease parameters. The model returns the expected number of COVID-19 deaths over time in each location, which is fitted against age-specific, COVID-19 mortality data. New data sources presented in this study are indicated in double-framed boxes.

S3.1 Infection model

The time evolution of SARS-CoV-2 infections is quantified in terms of a discrete-time age-specific renewal model. The discrete renewal model arises as the expected value of an age dependent branching process. The model extends a previous version to age-specific disease dynamics [56]. In the renewal equations, we model populations stratified by the 5-year age bands $\mathcal{A}$, such that

$$a \in \mathcal{A} = \Big\{[0-4], [5-9], \ldots, [75-79], [80-84], [85+]\Big\}, \tag{S21}$$

resulting in $A = 18$ population strata. We denote the number of new infections, c, on day t, in age band a, and location m as $c_{m,t,a}$, with $c_{m,t,a} \geq 0$ for all t, m, a. Here infections are taken to be both symptomatic and asymptomatic. We introduce a series of daily contact intensity matrices $\mathbf{C}_{mt}$ of dimension 18×18 in each location m. The time changing contact intensities $\mathbf{C}_{m,t}$ were modelled in a regression framework that uses as input pre-pandemic contact intensities, which will be presented in Section S3.4.2, as well as the age-specific mobility trends $X_{m,t,a}$ that are described in the Supplementary materials. Entry $\mathbf{C}_{m,t,a,a'}$ quantifies the expected number of contacts that one person in age group a has with persons of another age a' on day t in location m, which we refer to as contact intensity. We further consider the probability $\rho_{a'}$ that a contact with an infectious person leads to infection of one person in a'. We interpret $\rho_{a'}$ as a natural disease parameter that is region and time independent. We model $\rho_{a'}$ as the product of a constant baseline parameter ρ_0, and relative susceptibility parameters $\rho^S_{a'}$ for $a' \in \mathcal{A}$ through

$$\rho_{a'} = \rho_0 \times \rho^S_{a'} = \exp(\log \rho_0 + \log \rho^S_{a'}). \tag{S22}$$

To ensure a relative interpretation of the susceptibility parameters, we set $\rho^S_{a'} = 1$ for some age bands. Details are given in the Supplementary materials. This allows us to describe the time-varying reproduction number on day t from one infectious person in a in location m with

$$R_{m,t,a} = \sum_{a'} s_{m,t,a'}\, \rho_{a'}\, \mathbf{C}_{m,t,a,a'}, \tag{S23}$$

where $s_{m,t,a'}$ is the proportion of the population in location m and in age band a' that remains susceptible to SARS-CoV-2 infection. It is given by

$$s_{m,t,a'} = 1 - \frac{\sum_{s=1}^{t-1} c_{m,t,a'}}{N_{m,a'}}, \tag{S24}$$

where $N_{m,a'}$ denotes the population count in age group a' and location m. Extending the basic renewal model, we obtain similarly

$$c_{m,t,a'} \quad = \quad s_{m,t,a'}\rho_{a'} \sum_{a} \mathbf{C}_{m,t,a,a'} \left(\sum_{s=1}^{t-1} c_{m,s,a}\, g(t-s) \right) \tag{S25}$$

where g is the discretized generation time distribution as in [56]. This is because an individual of age a' in country m at time t makes contacts with individuals of age a at rate $\mathbf{C}_{m,t,a,a'}$, and these are successful with probability $\rho_{a'}$ if and only if 1) the individual in a' is susceptible, which is the case with probability $s_{m,t,a'}$, and 2) the individual in a is still infectious, which is the case with probability $g(t-s)$.

S3.2 Time-varying contact patterns

S3.2.1 Overview

Several studies have collected data on age-specific contact patterns in various settings across the United States prior to emergence of SARS-CoV-2 [58, 59, 60, 61]. However, little data are available on how contact patterns changed during the pandemic. These considerations prompted us to take a predictive approach. First, we used data from the Polymod study [62] to predict baseline contact matrices during the early part of the pandemic for each location, which we denote by $\mathbf{C}_m$. The pre-pandemic contact matrices quantify the expected number of contacts from one person in age band a with individuals in age band a' per day in location m, also known as contact intensities. Populations were stratified by 5-year age bands $a \in \mathcal{A}$ defined in (S21). Reflecting differences in contact patterns during weekdays and on weekends, distinct pre-pandemic contact matrices were generated for weekdays and weekends, $\mathbf{C}_m^{\text{wday}}$ and $\mathbf{C}_m^{\text{wend}}$. For simplicity we suppress the weekday and weekend notation in what follows, with all equations being analogous. Our approach is similar to those reported in [63, 64]. Details are presented in Section S3.2.2.

Second, we used the age-specific mobility trend data available for individuals aged $18+$ to predict time-varying contact intensities among individuals abve age 20. Overall, time changing contact intensities on day t in location m were modelled through

$$\mathbf{C}_{m,t,a,a'} = \eta_{m,t,a}\, \mathbf{C}_{m,a,a'}\, \eta_{m,t,a'}, \tag{S26}$$

where $a \in \{[20-25], \ldots, [85+]\}$ and $a' \in \{[20-25], \ldots, [85+]\}$. The multipliers $\eta_{m,t,a}$ describe the estimated effect of the age-specific mobility trends $X_{m,t,a}$ on changes in pre-pandemic contact matrices for each location. Since both the index person and the contacted individuals are changing their mobility over time, the multipliers are applied to the rows and columns of the contact intensity matrix. Details are presented in Section S3.2.3.

Third, we used data from two contact surveys conducted after nursery, kindergartens, and schools closures to specify contact intensities from and to individuals aged 0-19 during periods of school closure. Details are presented in Section S3.2.4.

Fourth, after state-wide school closures were no longer mandated, we reverted to the pre-pandemic contact intensities for children and teens aged 0-19, and estimated the extent to which disease relevant contacts from and to children and teens were reduced, and the extent to which disease relevant contacts between children and teens aged 0-19 were reduced. Details are presented in Section S3.2.4.

S3.2.2 Baseline contact intensity matrices prior to changes in mobility

We first obtained estimates of weekday and weekend contact matrices for 8 European countries from the Polymod contact survey [62]. Briefly, survey participants were recruited in such a way as to be broadly representative of the whole population in terms of geographical spread, age, and sex. Participants were asked to keep a diary of their contacts. The study included 7,290 participants recruited between May 12, 2005 and September 05, 2006. Contact intensities were estimated for Belgium, Germany, Finland, Italy, Luxembourg, the Netherlands, Poland, and the United Kingdom using the approach of [65], using code at the Github repository [66]. We index each of the European countries with e. The posterior median estimates of the number of individuals in age $\breve{a}'$ that were contacted per day by one individual in age $\breve{a}$ were extracted. Using the available methodology, populations were stratified in 1-year age bands. Figure S24 illustrates the estimated weekend and weekday contact intensity matrices for the 8 European countries.

To match the population stratification in the SARS-CoV-2 infection model, the estimated contact intensities at 1-year resolution were aggregated to 5-year resolution using

$$\mathbf{C}_{e,a,a'} = \sum_{\breve{a}\in a, \breve{a}'\in a'} \frac{N_{e,\breve{a}}}{\left(\sum_{\breve{a}\in a} N_{e,\breve{a}}\right)} \mathbf{C}_{e,\breve{a},\breve{a}'}, \tag{S27}$$

where $N_{e,\breve{a}}$ denotes the number of individuals in 1-year age band $\breve{a}$ in the corresponding European country e. The estimated contact intensities $\mathbf{C}_{e,a,a'}$ were real-valued and positive.

Following [63, 64], we constructed a predictive statistical model of contact intensities based on population demographics including the total population size, the number of individuals in age band a', the proportion of individuals in age band a', and population density. Regression models were fitted based on the $8 * 18 * 18 = 2,592$ estimates (S27) from the European-wide Polymod survey, separately for

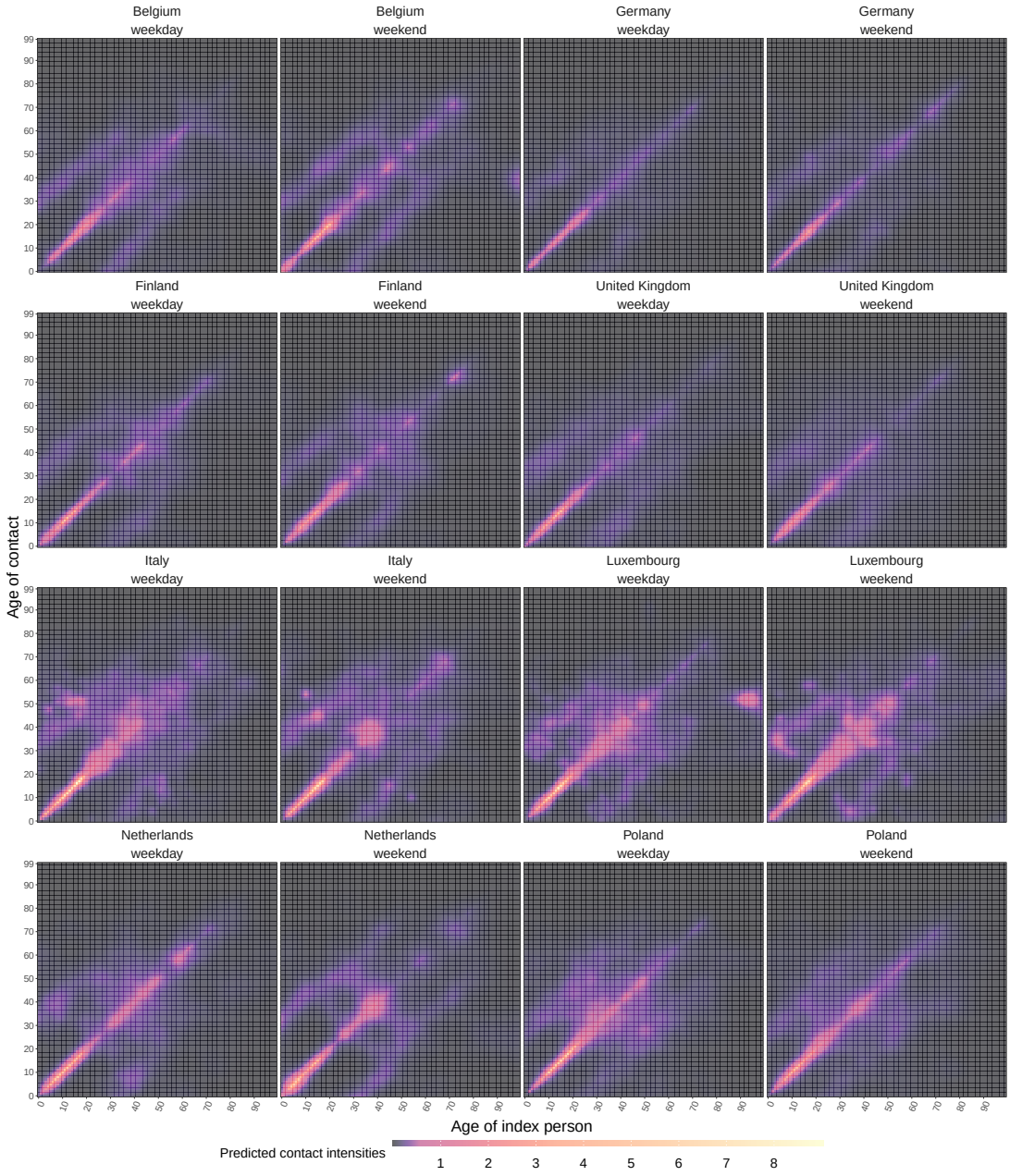

Figure S24: Estimated contact intensities for the 8 Polymod countries by weekday and weekend.

Figure S25: Predicted contact intensities versus Polymod estimates. Median predictions and 95% predictive intervals under model (S28) are shown in grey, and Polymod estimates are shown in blue.

Figure S26: Difference in contact intensities at weekends compared to weekdays. Locations ordered by population density.

weekdays and weekends. The chosen statistical model was of the form

$$\log \mathbf{C}_{e,a,a'} \sim \mathcal{N}(\mu_{e,a,a'}, \sigma^2) \tag{S28a}$$

$$\mu_{e,a,a'} = \theta_{a,a'} + \theta_1 \frac{N_{e,a'}}{N_e} + \theta_2 \log \frac{N_{e,a'}}{A_e}, \tag{S28b}$$

where $\theta_{a,a'}$ are pairwise age-specific baseline terms, $N_{e,a'}$ is the number of individuals in age band a' in location e, and A_e is the land area of location e in square kilometres. The least squares estimates of θ_1 and θ_2 were positive and highly significant for both weekday and weekend contact intensities, so that under model (S28) contact intensities with individuals of age a' increase as the proportion of the population of age a' increases, and as population density increases. The fits of model (S28) through the training data are illustrated in Fig. S25. The leave-one-out cross-validation mean absolute error associated with model (S28) was 0.361 and 84.1% of the variance was explained.

Baseline contact matrices for the 50 U.S states, the District of Columbia and New York City were then predicted using (S28). Fig. S4 shows the predicted baseline weekday contact matrices $\mathbf{C}_m$ for all locations. The predicted contact matrices are consistent with key characteristics of human contact patterns, including high number of contacts between children and teenagers of same age, parent-child interactions, broader workforce interactions, and child/parent-grandparent interactions. Fig. S5 illustrates location-specific differences in predicted contact intensities relative to the national average. In locations with young populations such as Alaska, the District of Columbia, Texas or Utah, lower contact intensities are predicted with individuals in young age groups when compared to the national average. Similarly, in locations with older populations such as Maine, higher contact intensities are predicted with individuals in older age groups when compared to the national average. Fig. S6 illustrates that locations with high population density such as the District of Columbia and New York City are predicted to have higher contact intensities compared to the national average. Fig. S26 compares predicted contact intensities on weekdays to those predicted for weekends. Predicted contact intensities were higher between children and the elderly individuals on weekends compared to weekdays for all locations.

S3.2.3 Time-varying contact intensities among individuals aged 20 and above

The time changing multipliers $\eta_{m,t,a}$ to the rows and columns of the pre-pandemic contact matrices were obtained through a regression model using the age-specific mobility trends (S3) as predictors. We matched the age stratification (S21) used in the model, with those from the original mobility trends through

$$X_{m,t,a} = X_{m,t,\tilde{a}}, \text{if } a \in \tilde{a}, \tag{S29}$$

where $\tilde{a} \in \tilde{\mathcal{A}}$ are the broader age strata in which the mobility data were reported, $[18-24], [25-34], [35-44], [45-54], [55-64], [65+]$.

To model heterogeneity in human behaviour and disease transmission after the rebound time in mobility trends, the mobility trends S29 were decomposed into three components. The three components

are a baseline mobility trend denoted by $X^{\text{base}}_{m,t,a}$, an eased mobility trend which we denote by $X^{\text{eased}}_{m,t,a}$, and an upswing multiplier that we denote by $X^{\text{upswing}}_{m,t,a}$. The decomposition satisfies the relation

$$X_{m,t,a} = X^{\text{base}}_{m,t,a} \times X^{\text{eased}}_{m,t,a} \times X^{\text{upswing}}_{m,t,a} \tag{S30}$$

for all m, t, and $a \in \{[20-24], \ldots, [85+]\}$. This approach is motivated by the general observation that since May/June 2020, when initial lock-downs were lifted, changes in overall mobility are less strongly correlated with changes in transmission risk [67, 68]. The above decomposition allows us to decouple the impact of mobility trends on changing contact intensities and transmission risk in the model in different stages of the COVID-19 epidemics.

Specifically, the base mobility trends, the eased mobility trends and multipliers were defined as

$$X^{\text{base}}_{m,t,a} = \begin{cases} X_{m,t,a} & \text{if } t < t^{\text{dip}}_m, \\ 1 & \text{if } t \geq t^{\text{dip}}_m, \end{cases} \tag{S31a}$$

$$X^{\text{eased}}_{m,t,a} = \begin{cases} 1 & \text{if } t < t^{\text{dip}}_m, \\ X_{m,t,a} & \text{if } t^{\text{dip}}_m \leq t < t^{\text{rebound}}_m, \\ \chi^{\text{wday}}_{m,a} & \text{if } t \geq t^{\text{rebound}}_m \text{ and } t \text{ is a weekday}, \\ \chi^{\text{wend}}_{m,a} & \text{if } t \geq t^{\text{rebound}}_m \text{ and } t \text{ is a weekend}, \end{cases} \tag{S31b}$$

$$X^{\text{upswing}}_{m,t,a} = \begin{cases} 1 & \text{if } t < t^{\text{dip}}_m, \\ 1 & \text{if } t^{\text{dip}}_m \leq t < t^{\text{rebound}}_m, \\ X_{m,t,a}/\chi^{\text{wday}}_{m,a} & \text{if } t \geq t^{\text{rebound}}_m \text{ and } t \text{ is a weekday}, \\ X_{m,t,a}/\chi^{\text{wend}}_{m,a} & \text{if } t \geq t^{\text{rebound}}_m \text{ and } t \text{ is a weekend}, \end{cases} \tag{S31c}$$

where $\chi^{\text{wday}}_{m,a}$ is the average of the mobility trend $X_{m,t,a}$ over the 5 weekdays before t^{rebound}_m, and $\chi^{\text{wend}}_{m,a}$ is the average of the mobility trend $X_{m,t,a}$ over the 4 weekend days before t^{rebound}_m. Fig. S27 illustrates the decomposed mobility trends for four locations.

With the decomposed mobility trends, we modelled the multipliers in (S26) that quantify the time evolution in contact intensities through

$$\eta_{m,t,a} = \exp\left(\log X^{\text{base}}_{m,t,a} + \beta^{\text{eased}}_m \log X^{\text{eased}}_{m,t,a} + \beta^{\text{upswing}}_{m,t,a} \log X^{\text{upswing}}_{m,t,a}\right), \tag{S32}$$

where β^{eased}_m is a spatially varying random effect across locations, and $\beta^{\text{upswing}}_{m,t,a}$ are structured random effects that vary in space, time and by age. The purpose of the eased mobility regression coefficient β^{eased}_m was to capture the effect of permanent reductions in contact patterns in the early phase of the pandemic. We reasoned that in populous areas, the same per cent reduction in venue check-ins may translate into a larger reduction in contact intensities than in less populous areas, and so allowed for different β^{eased}_m across locations. In addition, this choice was further motivated by the observation that

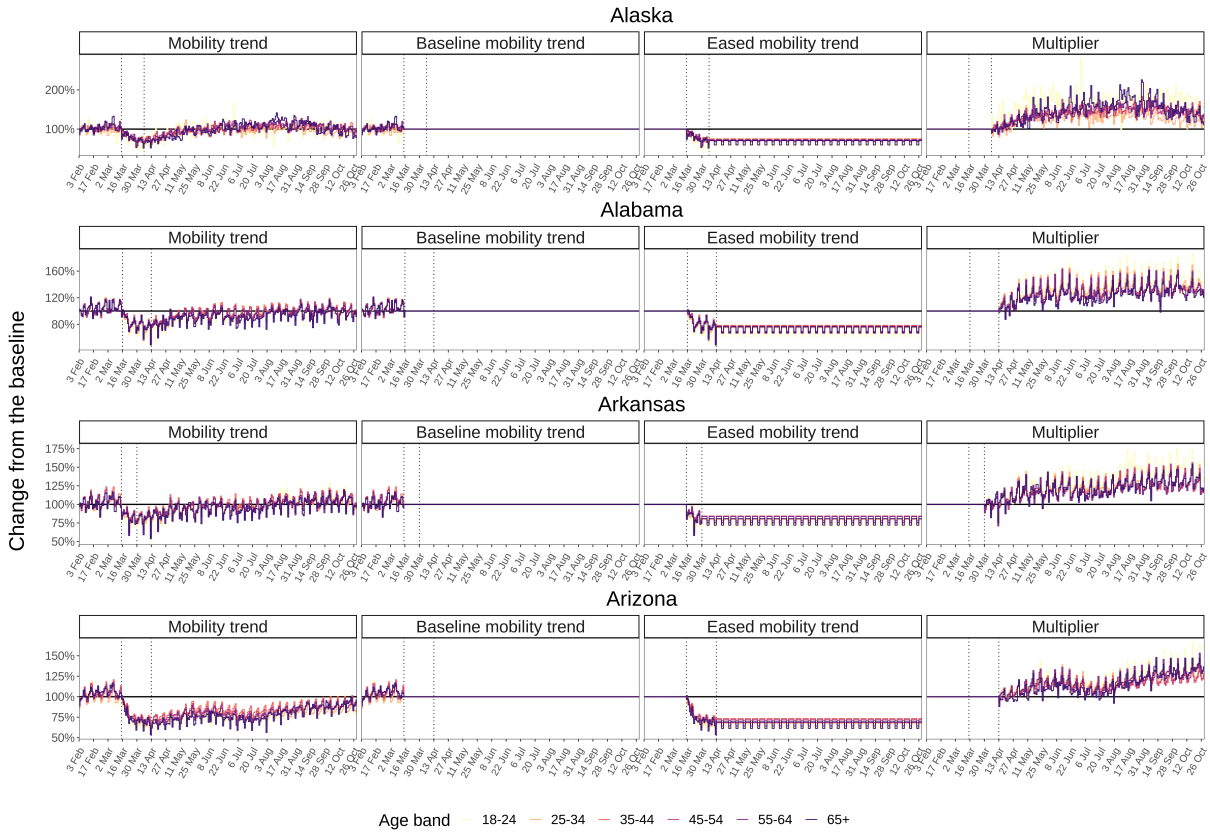

Figure S27: Decomposition of mobility trends, shown for 4 US locations. For each location, the change point in overall mobility trends was determined using a 10-day moving average. Age-specific mobility trends were then decomposed into eased mobility trends and multipliers as shown. The vertical dash lines indicate the change points when mobility dipped and began to rebound.

mobility trends dipped to varying extent across locations and showed systematically different trajectories after rebound, which suggested that the mobility trends cannot be interpreted on the same scale across states.

The purpose of the upswing regression coefficients $\beta^{\text{upswing}}_{m,t,a}$ was to capture longer-term effects after the initial reduction in contact patterns during the early phase of the pandemic. In general, because of the lower correlation of mobility trends with transmission risk after initial lock-downs, behaviour change and widely implemented non-pharmaceutical interventions [67, 68], we expected the upswing coefficients to be significantly lower than the coefficients associated with the initial declines. To model the substantial role of further behavioral factors such as contact duration, types of venues visited [69], or mask use [67, 70], the upwsing coefficients were allowed to vary in time independently for each location. Finally, to investigate the nature of resurgent epidemics and if resurgent epidemics are linked to changes in contact intensities and transmission risk from younger individuals, we further allowed the upswing

coefficients to vary by age. With this specification, we were able to formulate age-specific changes in transmission risk through differences in age-specific mobility trends (per cent change in venue check-ins by age groups) and further unobserved factors (e.g. age differences in contact duration, number of contacts per venue check-in, types of venues visited, protective measures in venues, etc.). A particular feature of the contact-and-infection model is that, when fitted to age-specific mobility and age-specific death data, all random effect regression parameters are identifiable across all states.

To illustrate the effect of the regression coefficients, consider the case that $\beta_m^{\text{eased}} = \beta_{m,t,a}^{\text{upswing}} = 0$. In this case, $\eta_{m,t,a} = 1$ and the contact intensities on day t are the same as at baseline after the dip date. If instead $\beta_m^{\text{eased}} = \beta_{m,t,a}^{\text{upswing}} = 1$, the contact intensities on day t from index persons scale with the observed mobility trend $X_{m,t,a}$. Finally, if $\beta_m^{\text{eased}} = 1$ and $\beta_{m,t,a}^{\text{upswing}} = 0$, the contact intensities on day t from index persons scale with the derived eased mobility trend $X_{m,t,a}^{\text{eased}}$ after the dip date.

S3.2.4 Contact intensities from and to children and teens aged 0-19 during periods of school closure and after re-opening

In the United States, closures of kindergartens, elementary schools, middle schools, and high schools were ordered at least at one level from April 4, 2020 [71]. School closure mandates have been continuously revised over the summer and fall of 2020. We retrieved dates on school closures and re-openings from the Oxford COVID-19 Government Response Tracker [71] and from Education Week, an independent K-12 education news organisation [72]. The data from Education Week are specific to government interventions targeting elementary, middle and high schools, and as such were preferred over the school intervention index of the Oxford COVID-19 Government Response Tracker, which also subsumed opening of colleges and universities.

In the model, we calculated periods of school closures and re-opening as follows. School closure dates were defined as the first week day on which state administrations mandated or recommended state-wide closures of elementary, middle, and high schools, and retrieved these dates from the Oxford COVID-19 Government Response Tracker [71]. School re-opening dates were defined as the first week day on which state administrations no longer mandated state-wide closure of elementary, middle, and high schools, and we retrieved these dates from Education Week [72]. We denote the time indices corresponding to state-wide school closures in location m by $t_m^{\text{school-close}}$, and the time indices corresponding to school re-opening in location m by $t_m^{\text{school-reopen}}$. Education Week data only started on August 19, 2020. If a school closure order was not in effect from the first day of the Education Week data, we set $t_m^{\text{school-reopen}}$ to August 24, 2020. By October 29, 2020, only the District of Columbia continued to mandate state-wide school closures [72]. Fig. S28 shows the timelines of schools status, across the US, as specified in our analysis.

To specify contact intensities from and to children and teens aged 0-19 during periods of school closure, we used data from two contact surveys conducted after kindergarten and school closures in response to accelerating COVID-19 epidemics in the UK and China [73, 54]. Fig. S29 compares the estimated contact intensities from one individual aged 0-19 using the contact surveys in Wuhan and Shang-

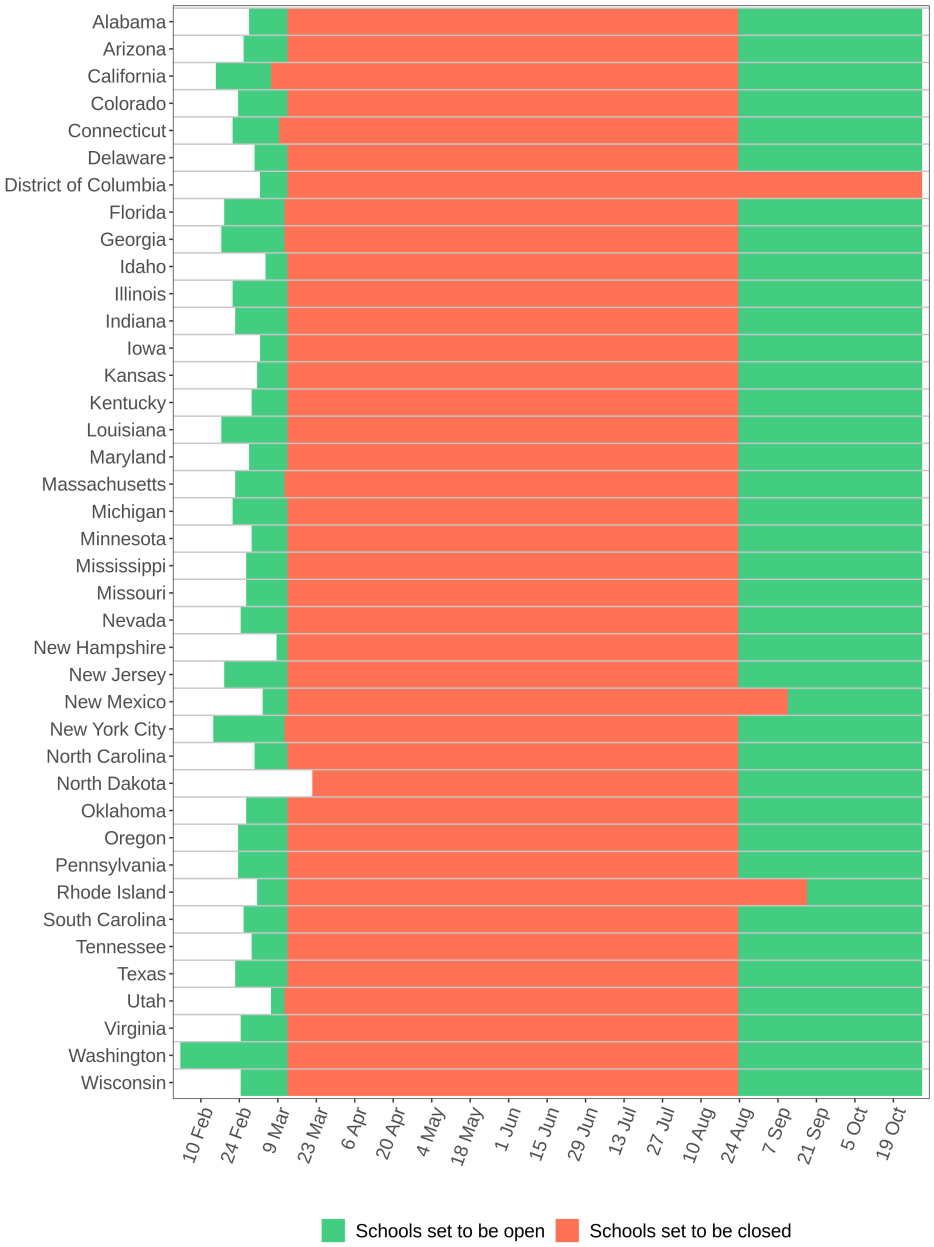

Figure S28: Timing of school closure periods in the model. School closure data were retrieved from [71] and school re-opening data were retrieved from [72]. School closure dates were defined as the first week day on which state administrations mandated or recommended state-wide closures of elementary, middle, and high schools. School re-opening dates were defined as the first week day on which state administrations no longer mandated state-wide closure of elementary, middle, and high schools.

hai before and during lockdown. Fig. S30 compares the estimated contact intensities to individuals aged 0-19. We plot the point estimates from the original report before lockdown to those during lockdown [54] (top row) and the ratio of the contact intensities during lockdown versus the corresponding contact intensities before lockdown (bottom row). During lockdown, the estimated, average number of daily peer-to-peer contacts from one individual aged 0-19 to individuals in the same age group was 0.09, corresponding to a contact intensity ratio of 0.01 across both cities. The total number of contacts from one individual aged 0-19 during the outbreak was 2.3, corresponding to a contact intensity ratio of 0.14 across both cities. The average number of contacts from one individual randomly chosen in the population to individuals in $0-19$ was 0.29 during lockdown, associated with a contact intensity ratio of 0.24. The contact survey of Jarvis and colleagues [73] in the UK included individuals aged $18+$, but interviewed individuals were also asked to report contacts to children and teenagers aged 0-17. During lockdown, the estimated, average number of daily peer-to-peer contacts from one individual older than 18 to children aged 0-17 was 0.78, corresponding to a contact intensity ratio of 0.25. In the model, we set the average daily contact intensities involving children and teens aged 0-19 during periods of school closure to the average daily contact intensities involving children and teens aged 0-19 that were observed during lockdown in Wuhan and Shanghai. We denote the observed, average daily contact intensities in Wuhan and Shanghai by

$$\mathbf{C}_{a,a'}^{lckdwn-0-19}, \tag{S33}$$

where either $a \in \{[0-4],[5-9],[10-14],[15-19]\}$ and a' is one of the 5-year age bands of the infection-and-contact model, or a is one of the 5-year age bands and $a' \in \{[0-4],[5-9],[10-14],[15-19]\}$.

After school closures were no longer mandated at state-level, children and teens aged 0-19 were modelled to resume their typical contact intensities on weekdays and weekends. Similarly as for the contact intensities between individuals aged $20+$ in Equation (S26), we modelled that these contact intensities could be reduced to lower levels through a multiplier η^{children} that acts on contacting children and teens, and on contacted children and teens. We further considered an additional multiplier γ acting on contacts between children and teens. In the absence of any mobility data for children and teens, these two parameters were estimated, and for this reason were also constant in time, across locations, and between children and teen age bands. The two variables reflect a number of factors mitigating disease spread, including temporary school closures in some school districts, impact of non-pharmaceutical interventions in schools with in-school teaching, reduced mobility of children and teens, or reduced infectiousness of SARS-Cov-2 from children and teens aged 0-19, and in practice we are unable to disentangle these factors. Specifically, after school closures periods, contact intensities were specified through

$$\mathbf{C}_{m,t,a,a'}^{\text{reopen-0-19}} = \begin{cases} \gamma\eta^{\text{children}}\mathbf{C}_{m,a,a'}\eta^{\text{children}} & \text{if } a<20, a'<20 \\ \eta^{\text{children}}\mathbf{C}_{m,a,a'}\eta_{m,t,a'} & \text{if } a<20, a'\geq 20 \\ \eta_{m,t,a'}\mathbf{C}_{m,a,a'}\eta^{\text{children}} & \text{if } a\geq 20, a'<20 \\ \eta_{m,t,a'}\mathbf{C}_{m,a,a'}\eta_{m,t,a'} & \text{if } a\geq 20, a'\geq 20 \end{cases} \tag{S34}$$

where $a, a' \in \mathcal{A}$, $\mathbf{C}_{m,a,a'}$ denote the pre-pandemic contact intensities, and $\eta_{m,t,a'}$ are the multipliers (S32).

In summary, for all time indices, the contact intensities involving children and teens aged 0-19 were modelled through

$$\mathbf{C}_{m,t,a,a'} = \begin{cases} \mathbf{C}_{m,a,a'} & \text{if } t < t_m^{\text{school-close}} \\ \mathbf{C}_{a,a'}^{lckdwn-0-19} & \text{if } t \in [t_m^{\text{school-close}}, t_m^{\text{school-reopen}} - 1] \\ \mathbf{C}_{m,t,a,a'}^{\text{reopen-0-19}} & \text{if } t \geq t_m^{\text{school-reopen}} \end{cases} \quad \text{(S35)}$$

where a or a' are one of $[0-4]$, $[5-9]$, $[10-14]$, $[15-19]$, $\mathbf{C}_{m,a,a'}$ is the prepandemic contact intensities described in Section S3.2.2, $\mathbf{C}_{a,a'}^{lckdwn-0-19}$ are the average contact intensities during lockdown of [54] that described in (S33), and $\mathbf{C}_{m,t,a,a'}^{\text{reopen-0-19}}$ are the contact intensities since school re-opening that are described in (S34).

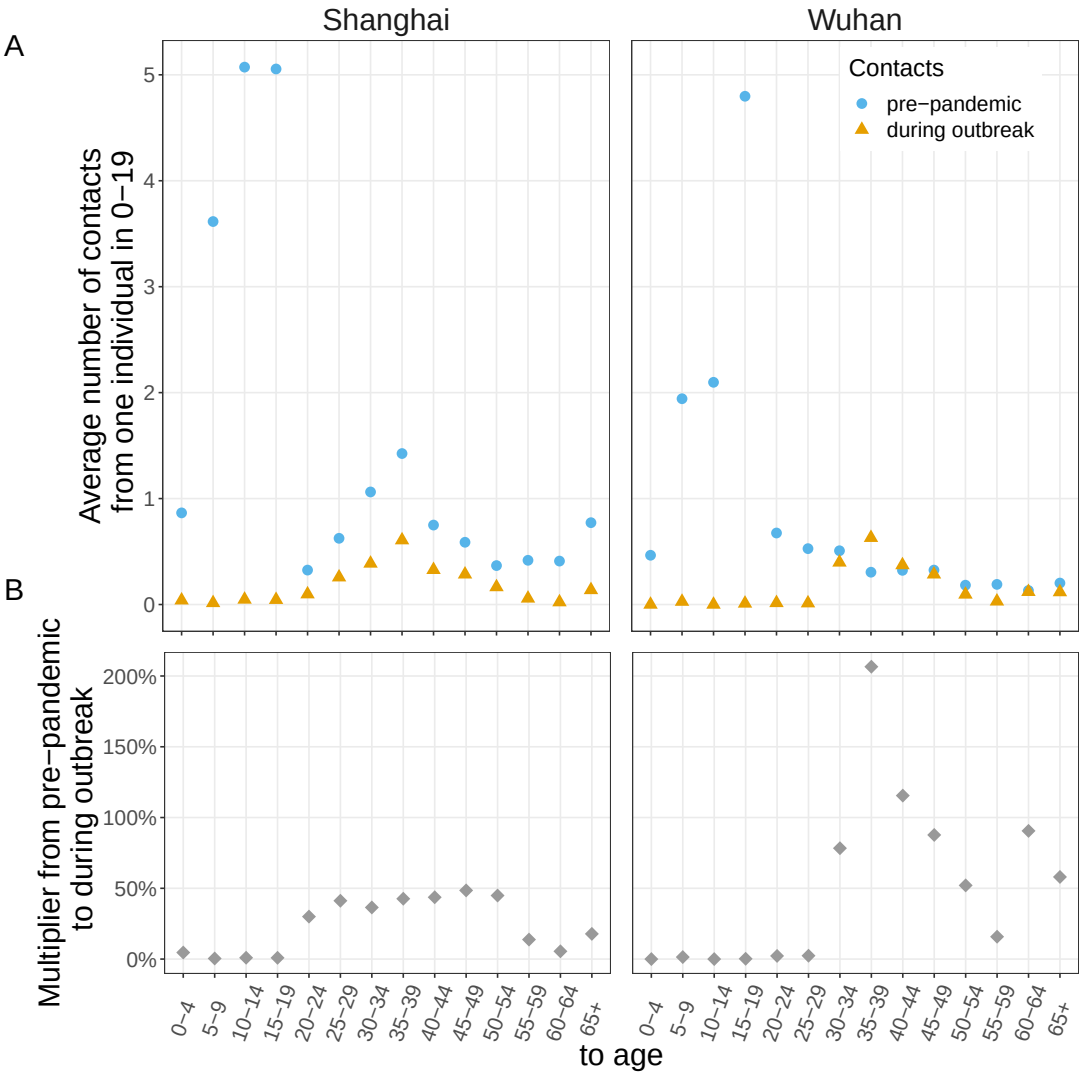

Figure S29: Estimated changes in contact intensities from one child or teen aged 0-19 during lockdown, Shanghai and Wuhan, China. Data from [54]. (**A**) Average number of contacts from one individual in 0-19 to individuals in 5-year age bands before (blue) and during (orange) lockdown. (**B**) Contact intensity ratio (grey).

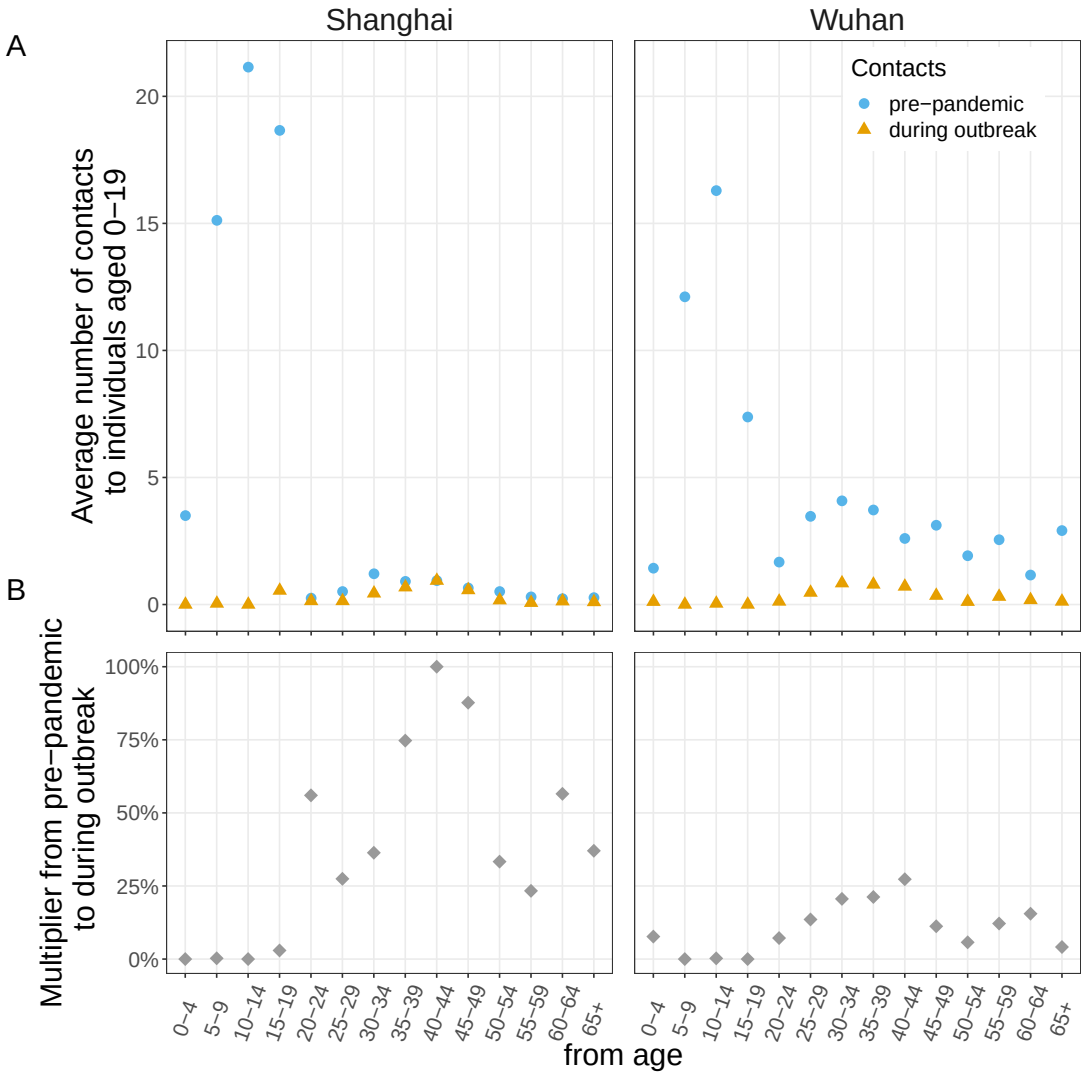

Figure S30: Estimated changes in contact intensities to children and teens aged 0-19 during lockdown, Shanghai and Wuhan, China. Data from [54]. (**A**) Average number of contacts from one individual in 5-year age bands to children aged 0-19 before (blue) and during (orange) lockdown. (**B**) Contact intensity ratio (grey).

S3.3 Likelihood

The contact-and-infection model is fitted to age-specific death counts for each location m, to overall death counts for time periods in which age-specific death counts are not available, and to overall case counts. To establish a link between the data and the expected number of cases $c_{m,t,a}$ (S25), we model the probability $H_{m,a}(t-s)$ that a person in age band a dies from SARS-CoV-2 infection before time $t-s$ after infection at time s in location m. We decompose the probability into the infection fatality ratio in location m, and age band a, $\pi_{m,a}$, and the infection-to-death distribution h that describes when a death occurs conditional on non-survival. We decompose $H_{m,a}(t-s)$ in this manner because estimates of both terms are available from the literature [5, 56]. Our model is

$$H_{m,a}(t-s) = \pi_{m,a} \int_0^{t-s} h(u)du, \tag{S36}$$

where $t-s$ is in continuous time and h integrates to 1. Using (S36), we can express the probability that a person in location m and age band a dies on day s after SARS-CoV-2 infection as

$$h_{m,s,a} = \int_{s-0.5}^{s+0.5} \pi_{m,a} h(u)du = \pi_{m,a} \int_{s-0.5}^{s+0.5} h(u)du \quad \forall s = 2, 3, \ldots, \tag{S37}$$

and $h_{m,1,a} = \pi_{m,a} \int_0^{1.5} h(u)du$ for $s = 1$. Using (S37), the expected number of COVID-19 deaths on day t in age band a in location m is

$$d_{m,t,a} = \sum_{s=1}^{t-1} c_{m,s,a} h_{m,t-s,a}, \tag{S38}$$

where $c_{m,s,a}$ is the expected number of new cases on day s in age band a in location m, (S25).

We link the expected number of deaths under the contact-and-infection model to the observed number deaths through an over-dispersed count model. For each location m, the data consist of daily, overall reported COVID-19 related deaths regardless of age until day $t_m^{\text{age-start}}$. For each location, time was re-scaled to 30 days prior to the first day when the cumulative number of deaths was 10 or larger. We denote the overall number of deaths on day t in location m by $y_{m,t}$ for $t < t_m^{\text{age-start}}$. From day $t_m^{\text{age-start}}$ onwards, COVID-19 related deaths are reported in location-specific age bands $b \in \mathcal{B}_m$. We denote the number of deaths on day t in location m in age band $b \in \mathcal{B}_m$ by $y_{m,t,b}$ for $t \geq t_m^{\text{age-start}}$. To match the location-specific death data, we aggregate the expected number of deaths under the self-renewal model to

$$d_{m,t} = \sum_{a \in \mathcal{A}} d_{m,t,a} \quad \forall t < t_m^{\text{age-start}} \tag{S39}$$

$$d_{m,t,b} = \sum_{a \in b} d_{m,t,a} \quad \forall t \geq t_m^{\text{age-start}}, \forall b \in \mathcal{B}_m. \tag{S40}$$

The log likelihood of the observed deaths then consists of three parts,

$$\ell^{\text{deaths}}(\mathbf{y}|\phi) = \sum_m \Bigg[\sum_{t_m^{\text{start}} \le t < t_m^{\text{age-start}}} \log \text{NegBin}\big(y_{m,t} \big| d_{m,t}, \phi\big) + \tag{S41a}$$

$$\sum_{t=t_m^{\text{age-start}}} \sum_{b \in \mathcal{B}_m} \log \text{NegBin}\Big(\sum_{s=1}^{t_m^{\text{age-start}}} y_{m,s,b} \Big| \sum_{s=1}^{t_m^{\text{age-start}}} d_{m,s,b}, \phi\Big) + \tag{S41b}$$

$$\sum_{t_m^{\text{age-start}} < t \le t_m^{\text{end}}} \sum_{b \in \mathcal{B}_m} \log \text{NegBin}\big(y_{m,t,b} \big| d_{m,t,b}, \phi\big) \Bigg], \tag{S41c}$$

where t_m^{start} is the first day on which at least 10 cumulated deaths were reported in location m, and t_m^{end} corresponds to the last day with overall death, or death by age data, see Table S10.

To ensure that the inferred, expected number of actual cases are larger than the number of reported cases in the following week, the contact-and-infection model is also fitted to the logarithm of weekly reported case data in each location, $z_{m,w}$. The case log likelihood was described in units of weeks to circumvent day-of-week effects. Plots suggested that the reported case data are subject to noise. For this reason we used a loess smoother through the reported data to predict the log weekly observed cases $\zeta_{m,w}$, which can be considered to follow a t-distribution with mean parameter $\mu_{m,w}^{\text{obs-cases}}$, standard deviation $\sigma_m^{\text{obs-cases}}$, and degrees of freedom $\nu_m^{\text{obs-cases}}$, that are returned by the loess smoother. The log likelihood of the observed case data was then specified through

$$\ell^{\text{obs-cases}}(\zeta) = \sum_m \sum_{w_m^{\text{start}} \le w < w_m^{\text{end}}} \log Pr(\zeta_{m,w} < \log c_{m,w-1}), \tag{S42}$$

where w_m^{start} denotes the week in which at least 10 cumulated deaths were reported in location m, and w_m^{end} denotes the week with the last day of death data.

To ensure that the inferred, expected number of actual cases among school-aged children are larger than reported cases in schools and smaller than a multiple of the reported cases, the contact-and-infection model is further fitted to reported attack rates among school-aged children and teens aged 5-18, u_m, during state-specific observation periods, $t_m^{\text{att-start}}$ to $t_m^{\text{att-end}}$. To calculate attack rates among school-aged children and teens, we first identified schools in location m that reported student case counts K1-K12 during the entire observation period and for which enrolment sizes could be retrieved from the Common Core of Data America's School database [74]. Then, attack rates were calculated by summing reported student cases across schools in the period $t_m^{\text{att-start}}$ to $t_m^{\text{att-end}}$, and dividing the total by the sum of student enrolment sizes in the same schools. In the model, expected attack rates among school-aged children were calculated through

$$\begin{aligned} a_m = &\Big(\sum_{t_m^{\text{att-start}} \le t \le t_m^{\text{att-end}}} c_{m,t,[5-9]} + c_{m,t,[10-14]} + \frac{4}{5} c_{m,t,[15-19]} \Big) \Big/ \\ &\Big(N_{m,[5-9]} + N_{m,[10-14]} + \frac{4}{5} N_{m,[15-19]} \Big), \end{aligned} \tag{S43}$$

where $c_{m,t,a}$ are the new infections in location m on day t in age band a, and $N_{m,a}$ are the number of individuals in location m in age band a. The log likelihood of the reported attack rates among school-aged children and teens was then specified through

$$\ell^{\text{school-att-lower}}(u|a) = \sum_m \log \text{Normal-cdf}(a_m; u_m, u_m/10). \tag{S44}$$

We further assumed that the expected attack rates among school-aged children and teens should not be higher than a multiple ξ of the reported attack rates u_m, and added the constraint

$$\ell^{\text{school-att-upper}}(u|a) = \sum_m \log \text{Normal-ccdf}(a_m; (\xi u_m), (\xi u_m)/10), \tag{S45}$$

where ξ was varied between 2 and 10, and $\xi = 6$ was used in the central analysis; see Section S3.4.3.

S3.4 Inputs and prior distributions on model parameters

The contact-and infection model has the following inputs, which we consider fixed, and model parameters, which we consider unknown and estimate (see Table S9). The total number of estimated parameters in the model is $31 + (N_V + 7) \times M$, where M is the number of locations and N_V is the number of bi-weekly intervals, which for the central analysis amounted to 771 estimated parameters.

S3.4.1 Infection dynamics

Initial number of infections. For each location, the number of SARS-CoV-2 infections in the first 6 days of the observation period among individuals aged 20-54 are given the prior distribution

$$\log c_{m,t,[20-54]} \sim \mathcal{N}(4.85, 0.4^2), \quad t = 1, \ldots, 6 \tag{S46}$$

Recall that the observation period starts 30 days prior to the first day when the cumulative number of deaths in location m was 10 or larger. A priori we thus expect on average 125 infections to have occurred in the first 6 days among individuals aged 20-54 years. The new infections are then equally distributed across the corresponding age bands,

$$c_{m,t,a} = \begin{cases} c_{m,t,[20-54]}/7 & \text{if } a \in \mathcal{A}_0 \\ 0 & \text{otherwise,} \end{cases} \tag{S47}$$

where $\mathcal{A}_0 = \{[20-24], [25-59], [30-34], [35-39], [40-44], [45-49], [50-54]\}$ and $t = 1, \ldots, 6$.

Infection parameters. The infection parameters described in (S22) comprise the baseline infection parameter in location m, ρ_{0m} (real-valued), as well as relative susceptibility (S) parameters ρ^S (vector-valued of length A).

Table S10: Dates with overall and death by age data included in the likelihood. Our analysis include 40 locations with death by age.

Location	Dates with overall data	Dates with death by age data	Number of age groups
Alabama	March 29, 2020 - May 02, 2020	May 03, 2020 - October 29, 2020	6
Alaska	-	-	-
Arizona	March 27, 2020 - May 12, 2020	May 13, 2020 - October 29, 2020	5
Arkansas	-	-	-
California	March 17, 2020 - May 12, 2020	May 13, 2020 - October 29, 2020	4
Colorado	March 25, 2020 - March 25, 2020	March 26, 2020 - October 29, 2020	9
Connecticut	March 23, 2020 - April 04, 2020	April 05, 2020 - October 29, 2020	9
Delaware	March 31, 2020 - May 11, 2020	May 12, 2020 - October 29, 2020	6
District of Columbia	April 02, 2020 - April 12, 2020	April 13, 2020 - October 29, 2020	8
Florida	March 20, 2020 - March 26, 2020	March 27, 2020 - October 29, 2020	10
Georgia	March 19, 2020 - May 08, 2020	May 09, 2020 - October 29, 2020	18
Hawaii	-	-	-
Idaho	April 04, 2020 - June 15, 2020	June 16, 2020 - October 29, 2020	8
Illinois	March 23, 2020 - May 13, 2020	May 14, 2020 - October 29, 2020	8
Indiana	March 24, 2020 - May 12, 2020	May 13, 2020 - October 29, 2020	8
Iowa	April 02, 2020 - May 12, 2020	May 13, 2020 - October 29, 2020	5
Kansas	April 01, 2020 - June 01, 2020	June 02, 2020 - October 29, 2020	9
Kentucky	March 30, 2020 - May 12, 2020	May 13, 2020 - October 29, 2020	9
Louisiana	March 19, 2020 - May 11, 2020	May 12, 2020 - October 29, 2020	7
Maine	-	-	-
Maryland	March 29, 2020 - May 13, 2020	May 14, 2020 - October 29, 2020	9
Massachusetts	March 24, 2020 - April 19, 2020	April 20, 2020 - October 29, 2020	8
Michigan	March 23, 2020 - March 23, 2020	March 24, 2020 - October 29, 2020	8
Minnesota	March 30, 2020 - May 20, 2020	May 21, 2020 - October 29, 2020	11
Mississippi	March 28, 2020 - September 29, 2020	September 30, 2020 - October 29, 2020	7
Missouri	March 28, 2020 - May 12, 2020	May 13, 2020 - October 29, 2020	8
Montana	-	-	-
Nebraska	-	-	-
Nevada	March 26, 2020 - June 06, 2020	June 07, 2020 - October 29, 2020	8
New Hampshire	April 08, 2020 - June 06, 2020	June 07, 2020 - October 29, 2020	9
New Jersey	March 20, 2020 - May 24, 2020	May 25, 2020 - October 29, 2020	7
New Mexico	April 03, 2020 - April 03, 2020	April 04, 2020 - October 29, 2020	8
New York	-	-	-
New York City	March 16, 2020 - June 30, 2020	July 01, 2020 - October 29, 2020	5
North Carolina	March 31, 2020 - May 19, 2020	May 20, 2020 - October 29, 2020	6
North Dakota	April 21, 2020 - May 13, 2020	May 14, 2020 - October 29, 2020	9
Ohio	-	-	-
Oklahoma	March 28, 2020 - May 12, 2020	May 13, 2020 - October 29, 2020	6
Oregon	March 25, 2020 - June 04, 2020	June 05, 2020 - October 29, 2020	9
Pennsylvania	March 25, 2020 - June 06, 2020	June 07, 2020 - October 29, 2020	8
Rhode Island	April 01, 2020 - May 31, 2020	June 01, 2020 - October 29, 2020	9
South Carolina	March 27, 2020 - May 13, 2020	May 14, 2020 - October 29, 2020	9
South Dakota	-	-	-
Tennessee	March 30, 2020 - April 08, 2020	April 09, 2020 - October 29, 2020	9
Texas	March 24, 2020 - July 27, 2020	July 28, 2020 - October 29, 2020	11
Utah	April 06, 2020 - June 16, 2020	June 17, 2020 - October 29, 2020	6
Vermont	-	-	-
Virginia	March 26, 2020 - April 20, 2020	April 21, 2020 - October 29, 2020	9
Washington	March 04, 2020 - June 07, 2020	June 08, 2020 - October 29, 2020	5
West Virginia	-	-	-
Wisconsin	March 26, 2020 - March 26, 2020	March 27, 2020 - October 29, 2020	9
Wyoming	-	-	-

To place a prior density on $\rho_{0,m}$, we consider prior estimates on the basic reproduction number [75], and specify the following prior distribution on the basic reproduction number $R_{0,m}$ in location m,

$$\log R_{0,m} \sim \mathcal{N}(0.98, 0.2^2), \tag{S48a}$$

where the corresponding prior mean and 95% confidence intervals, $2.7\ [1.6 - 3.9]$, are based on the meta-analysis of [53]. To obtain $\rho_{0,m}$, we re-scale $R_{0,m}$ by the average number of contacts of one person in location m at baseline,

$$\rho_{0,m} = R_{0,m}/\bar{C}_m \tag{S49a}$$

$$\bar{C}_m = \sum_a p_{m,a} \sum_{a'} \mathbf{C}^{\text{wday}}_{m,a,a'}, \tag{S49b}$$

where $\mathbf{C}^{\text{wday}}_m$ is the baseline weekday contact matrix defined in S3.4.2 and $p_{m,a}$ is the proportion of the population of location m in age band a.

To place prior densities on the relative susceptibility parameters, we used available data from contact tracing and testing in mainland China [54]. Based on the available data, we considered relative susceptibility parameters for the age bands $[0 - 14]$, $[15 - 64]$ and $[65+]$, and specified the prior densities

$$\log \rho^S_{[0-14]} \sim \mathcal{N}(-1.0702, 0.2170^2) \tag{S50a}$$

$$\log \rho^S_{[65+]} \sim \mathcal{N}(0.3828, 0.1638^2), \tag{S50b}$$

where the hyperparameters were obtained by fitting a lognormal distribution to the reported 95% confidence intervals in [54] with the `lognorm` R package, version 0.1.6 [76].

The log susceptibility parameters for age band $[15 - 64]$ were set to 0, so that ρ^S is interpreted relative to infection dynamics from/to individuals in age band $[15 - 64]$. Considering the 18 age bands of the COVID-19 transmission model, the age-specific relative susceptibility parameters were set to

$$\log \rho^S_a = \begin{cases} \log \rho^S_{[0-14]} & \text{if } a \in [0 - 14] \\ \log \rho^S_{[15-64]} & \text{if } a \in [15 - 64] \\ \log \rho^S_{[65+]} & \text{if } a \in [65+]. \end{cases}, \tag{S51}$$

Discretised generation time distribution. The generation time distribution (S25) was kept fixed. Using estimates of [55], we specified the continuous-time version

$$g^{CT}(s) = \text{Gamma}(6.5, 0.62). \tag{S52}$$

Equation (S52) was then discretised to units of days,

$$g(s) = \int_{s-0.5}^{s+0.5} g^{CT}(u)\, du \quad \forall s = 2, 3, \ldots \tag{S53}$$

and $g(1) = \int_0^{1.5} g^{CT}(u)\, du$ for $s = 1$. This input specification is the same as in the base model [56].

S3.4.2 Time changing contact patterns

Baseline age-specific contact matrices The pre-pandemic contact intensity matrices were constructed as described in the Supplementary materials, and are illustrated in Figs. S4-S26.

Mobility trends (percent reduction in venue visits by age). Changes in contact intensities were described through a random effects regression model with decomposed, age- and location-specific mobility trends as covariates and additional location, age, and time-specific random effects. The mobility trend data used in this study are described in Section S1.2, and capture percent changes in venue visits of individuals in different age groups over time. The decomposition into baseline mobility trends $X^{\text{base}}_{m,t,a}$, eased mobility trends $X^{\text{eased}}_{m,t,a}$ and upswing multipliers $X^{\text{upswing}}_{m,t,a}$ on day t in location m and age band a is defined in (S31), and was used to reflect lower correlations between mobility trends and transmission risk after initial lock-downs.

Mobility trend regression coefficients and further random effects. Equations (S26) and (S32) describe our model of changing contact intensities,

$$\begin{aligned}
\mathbf{C}_{m,t,a,a'} &= \eta_{m,t,a}\, \mathbf{C}_{m,a,a'}\, \eta_{m,t,a'} \\
\eta_{m,t,a} &= \exp\left(\log X^{\text{base}}_{m,t,a} + \beta^{\text{eased}}_{m} \log X^{\text{eased}}_{m,t,a} + \beta^{\text{upswing}}_{m,t,a} \log X^{\text{upswing}}_{m,t,a} \right).
\end{aligned}$$

The purpose of the eased mobility regression coefficient β^{eased}_{m} was to capture the effect of permanent reductions in contact patterns in the early phase of the pandemic. We reasoned that in populous areas, the same per cent reduction in venue check-ins may translate into a larger reduction in contact intensities than in less populous areas, and so allowed for different β^{eased}_{m} across locations. In addition, this choice was further motivated by the observation that mobility trends dipped to varying extent across locations and showed systematically different trajectories after rebound, which suggested that the mobility trends cannot be interpreted on the same scale across states. Specifically, we specified the spatial random effect through,

$$\begin{aligned}
\beta^{\text{eased}}_{m} &\sim \mathcal{N}(\beta^{\text{eased}}, \sigma^2_{\text{eased}}) \\
\beta^{\text{eased}} &\sim \mathcal{N}(0, 1) \\
\sigma_{\text{eased}} &\sim \text{Exponential}(1.5).
\end{aligned} \tag{S54}$$

The upswing random effects $\beta^{\text{upswing}}_{m,t,a}$ are intended to capture further disease-relevant, unobserved behavioral factors such as contact duration, types of venues visited, or mask use [67, 70]. In addition, the random effects were specified to investigate the nature of resurgent epidemics and if resurgent epidemics are linked to changes in contact intensities and transmission risk from younger individuals. A particular feature of the contact-and-infection model is that, when fitted to age-specific mobility and

age-specific death data, all random effect regression parameters are identifiable across states. Specifically, we specified the upswing random effects through

$$\beta^{\text{upswing}}_{m,t,a} = (\beta^{\text{upswing-base}} + \beta^{\text{upswing-age}}_{m,a}) \times \beta^{\text{upswing-time}}_{m,t}. \tag{S55}$$

In (S55), $\beta^{\text{upswing-base}}$ acts as a baseline effect of mobility increases since the rebound time on contact intensities,

$$\beta^{\text{upswing-base}} \sim \mathcal{N}(0, 1), \tag{S56}$$

which a priori we expected to be lower than the average effect associated with initial reductions in mobility trends, β^{eased}. The time-specific random effects $\beta^{\text{upswing-time}}_{m,t}$ are, independently for each location, specified as a bi-weekly AR(1) process centered at zero. This allows the mobility trends (percent reduction in venue check-ins for each age group) to have different effects on contact intensities and transmission risk over consecutive two week intervals in each location, and as such can be interpreted as unobserved factors that modulate how changes in venue check-ins translate into transmission risk over time. Specifically,

$$\begin{aligned}
&\beta^{\text{upswing-time}}_{m,t} = \varepsilon_{m,\lfloor c(m,t)/2 \rfloor},\\
&\varepsilon_{m,1} \sim \mathcal{N}_{[0,\infty)}(0, 0.025^2),\\
&\varepsilon_{m,v} \sim \mathcal{N}_{[0,\infty)}(\varepsilon_{m,v-1}, \sigma^2_\varepsilon) \text{ for } v > 1,\\
&\log \sigma_\varepsilon \sim \mathcal{N}(-1.2, 0.2^2),
\end{aligned} \tag{S57}$$

where $\mathcal{N}_{[a,b)}$ denotes a truncated normal distribution between a and b and $c(t)$ is a function that maps the time indices in location m to calendar weeks. The random effects were constrained to positive values in order to escape strong correlations with $\beta^{\text{upswing-base}}$ in the joint posterior density and facilitate mixing. The variance parameter σ_ε was a priori given a mean of 0.3 to favour smooth time trends in $\beta^{\text{upswing-time}}_{m,t}$ over spontaneous changes. The age-specific random effects $\beta^{\text{upswing-age}}_{m,a})$ were added to the model to test for the presence of age-specific unobserved factors among individuals aged 20-49 with a net positive effect on disease relevant contact intensities and transmission risk. Together with the time effects $\beta^{\text{upswing-time}}_{m,t}$, the age-specific unobserved factors among individuals aged 20-49 can in principle have occurred within any two week interval after mobility trends started to rebound. We allowed for heterogeneity in the age-specific effects among individuals aged 20-49 across locations through

$$\begin{aligned}
\beta^{\text{upswing-age}}_{m,[20-49]} &\sim \text{Exp}(\beta^{\text{upswing-age}}_{[20-49]})\\
\beta^{\text{upswing-age}}_{[20-49]} &\sim \text{Exp}(0.1),
\end{aligned} \tag{S58}$$

and then specified

$$\beta^{\text{upswing-age}}_{m,a} = \begin{cases} \beta^{\text{upswing-age}}_{m,[20-49]} & \text{if } a \in [20-49] \\ 0 & \text{otherwise.} \end{cases} \tag{S59}$$

More general versions of this model with age-specific random effects for individuals aged 20-49, 50-74, and $75+$ were also considered, however the posterior distributions of the age-specific random effects

associated with individuals aged 50-74 and $75+$ were close to zero and left out from the final model for computational tractability. More general versions of this model with age-specific random effects for individuals aged 20-34 and 35-49 resulted in strong correlations between the two parameters, indicating that we are unable to separate effects attributable to both age groups based on the current data.

Reduction in contacts from and to school-aged children after school re-opening. The parameter η^{school} in (S34) reduces the number of contacts from and to school aged children from pre-pandemic levels, and was associated with the prior density

$$\eta^{\text{school}} \sim \text{Uniform}(0.1, 1.0). \tag{S60}$$

The parameter γ in (S34) captures additional reductions in disease-relevant contacts between children and teens was associated with the prior density

$$\log \gamma \sim \mathcal{N}(0, 0.35). \tag{S61}$$

S3.4.3 Likelihood

Location and age-specific infection fatality ratio. The contact-and-infection model back-calculates past infections in age groups from observed deaths in age groups via the age specific infection fatality ratio as described in Equations (S37-S38),

$$d_{m,t,a} = \sum_{s=1}^{t-1} c_{m,s,a} h_{m,t-s,a} \tag{S62}$$

$$h_{m,1,a} = \pi_{m,a} \int_0^{1.5} h(u)du \tag{S63}$$

$$h_{m,s,a} = \pi_{m,a} \int_{s-0.5}^{s+0.5} h(u)du \quad \forall s = 2, 3, \ldots, \tag{S64}$$

where $d_{m,t,a}$ is the expected number of COVID-19 deaths on day t in age band a in location m, $c_{m,s,a}$ is the expected number of new cases on day s in age band a in location m, h is the discretised infection-to-death distribution that describes when a death occurs conditional on non-survival, and $\pi_{m,a}$ is the infection fatality ratio in location m and age band a. Our specification of the age-specific infection fatality ratio relies on a recent meta-analysis across 113 meta-regression observations of infection fatality ratios [5], and further allows for deviations across US locations in terms of location and age-specific random effects. Specifically, we decompose the age-specific infection fatality ratio into

$$\pi_{m,a} = \text{exp}(\log \pi_a^{\text{IFR-meta}} + \log \delta_{m,a}^{\text{IFR}}), \tag{S65}$$

where $\pi_a^{\text{IFR-meta}}$ are the estimates taken from the meta-analysis of [5], and $\log \delta_{m,a}^{\text{IFR}}$ are location-specific random effects to account for departures from the meta-regression estimate on a subset of age classes.

Table S11: Hyperparameters of the prior density on age-specific infection fatality ratios, equation (S66)**.**

	$[0-4]$	$[5-9]$	$[10-14]$	$[15-19]$	$[20-24]$	$[25-29]$
μ_a	-11.8588167	-11.2527085	-10.6468661	-10.041283	-9.4359533	-8.830871
σ_a	0.1657816	0.1513949	0.1374366	0.1240003	0.11122	0.0992908
	$[30-34]$	$[35-39]$	$[40-44]$	$[45-49]$	$[50-54]$	$[55-59]$
μ_a	-8.2260307	-7.6214275	-7.0170568	-6.4129146	-5.8089986	-5.2053077
σ_a	0.0884956	0.0792359	0.0720426	0.0675226	0.0661851	0.068205
	$[60-64]$	$[65-69]$	$[70-74]$	$[75-79]$	$[80-84]$	$[85+]$
μ_a	-4.6018431	-3.9986079	-3.3956061	-2.7928423	-2.1903216	-1.2062531
σ_a	0.0733224	0.0809885	0.0906026	0.1016588	0.1137825	0.1364627

To construct a prior distribution for $\log \pi_a^{\text{IFR-meta}}$, we took the numerical estimates of the 95% credible intervals associated with the posterior predictive infection fatality ratios in [5], and fitted log-normal distributions using the `lognorm` R package, version 0.1.6, [76]. The resulting hyper-parameters of the prior densities

$$\log \pi_a^{\text{IFR-meta}} \sim \mathcal{N}(\mu_a^{\text{IFR-meta}}, {\sigma_a^{\text{IFR-meta}}}^2), \tag{S66}$$

for the 18 increasing age bands in this study are reported in Table S11. For each location, the model allows for potentially larger infection fatality ratios compared to the overall meta-analysis estimate in terms of 3 age bands,

$$\log \delta_{m,[20-49]}^{\text{IFR}} \sim \text{Exp}(\delta_{[20-49]}^{\text{IFR}}), \tag{S67a}$$

$$\log \delta_{m,[50-69]}^{\text{IFR}} \sim \text{Exp}(\delta_{[50-69]}^{\text{IFR}}), \tag{S67b}$$

$$\log \delta_{m,[70+]}^{\text{IFR}} \sim \text{Exp}(\delta_{[70+]}^{\text{IFR}}), \tag{S67c}$$

$$\delta_{[20-49]}^{\text{IFR}}, \delta_{[50-69]}^{\text{IFR}}, \delta_{[70+]}^{\text{IFR}} \sim \text{Exp}(0.1). \tag{S67d}$$

The random-effect parameters were restricted to capture positive departures from the meta-analysis estimates in order reduce correlations in the joint posterior distribution between the random effects and other model parameters, and facilitate computational inference. Then, the age-specific random effects $\log \delta_{m,a}^{\text{IFR}}$ for each of the 18 age bands of the contact-and-infection model were set to

$$\log \delta_{m,a}^{\text{IFR}} = \begin{cases} \log \delta_{m,[20-49]}^{\text{IFR}} & \text{if } a \in [20-49] \\ \log \delta_{m,[50-69]}^{\text{IFR}} & \text{if } a \in [50-69] \\ \log \delta_{m,[70+]}^{\text{IFR}} & \text{if } a \in [70+] \\ 0 & \text{otherwise.} \end{cases} \tag{S68}$$

Infection-to-death distribution. The infection-to-death distribution h in (S36) was kept fixed. Following [77, 78], we first specified the infection-to-onset-of-symptoms distribution and the onset-to-death, and modelled the infection-to-death distribution as the sum of both components through

$$h(s) = \text{Gamma}(s; 5.1, 0.86) + \text{Gamma}(s; 17.8, 0.45), \tag{S69}$$

where s is in continuous time. This input specification is the same as in the base model [56].

Overdispersion parameter. The prior distribution on the overdispersion parameter ϕ in the Negative Binomial observation model (S41) was given by the prior density

$$\phi \sim \mathcal{N}_{[0,\infty)}(0, 5). \tag{S70}$$

Upper bound on attack rates among school-aged children and teens. The upper bound ξ on attack rates among school-aged children and teens in Equation (S45) was kept fixed in analyses, however different upper bounds between $\xi = 2$ to $\xi = 10$ were explored. The lower value $\xi = 2$ was based on previous findings that 50% of infected children and teens may be asymptomatic [57], so that approximately every second infection among children and teens might be detectable through testing of individuals showing symptoms. The upper bound $\xi = 10$ was motivated by the fact that estimated population-level ratios of reported versus actual cases were typically below 10 [79]. For the central analysis, we considered the population-level ratios of reported cases versus the posterior median of actual cases across locations in the model, which was typically between 3-6 since June 2020. On this basis we chose $\xi = 6$, and interpret it as a likely overestimate and likely upper bound on the actual attack rate among school-aged children and teens.

S3.5 Computational inference

The Bayesian hierarchical model was fit with CmdStan release 2.23.0 (22 April 2020), using an adaptive Hamiltonian Monte Carlo (HMC) sampler [80]. 8 HMC chains were run in parallel for $2,000$ iterations, of which the first $1,500$ iterations were specified as warm-up. Calculations for each HMC chain were distributed over 1 processor per U.S location (state or metropolitan area) with CmdStan's `reduce_sum` functionality. Posterior convergence was assessed using the Rhat statistics and by diagnosing divergent transitions of the sampler. There are 4,000 iterations after burn-in across 8 chains, and 10 parameters with the lowest effective sample sizes were assessed. Those effective sample sizes of are from 212 to 499, and Rhats are from 1.009 to 1.0321. There were 4092 divergent transitions, and that the average posterior step size was around 0.003. The pair plot of parameters for New York City is in Fig. S31.

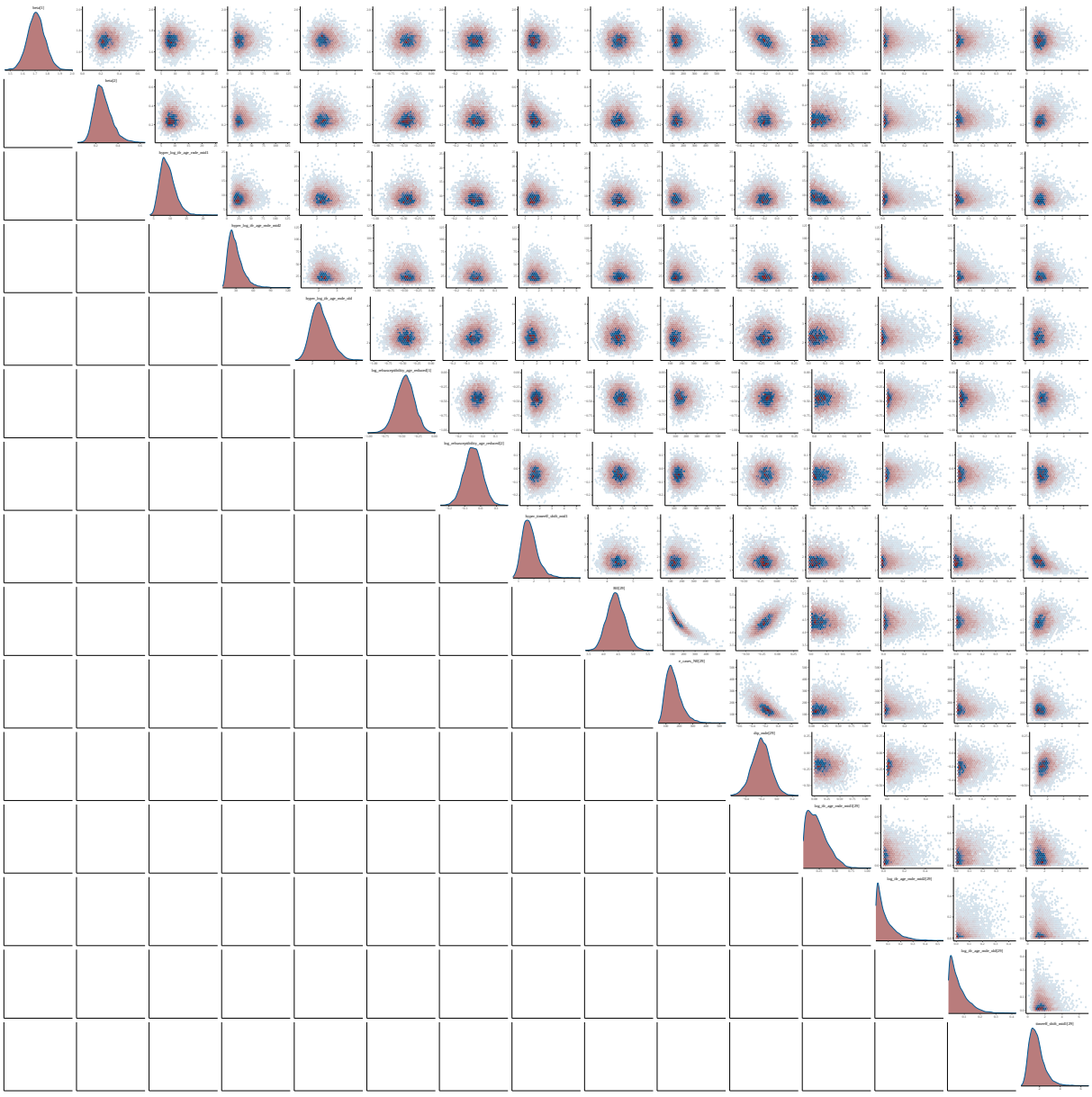

Figure S31: Pair plots of the joint posterior distribution of the model parameters for New York City.

DOI: https://doi.org/10.25561/82551

S3.6 Generated quantities

Age stratification for reporting purposes. In the manuscript results are reported using the following 8 age bands

$$d \in \mathcal{D} = \Big\{[0-9], [10-19], [20-34], [35-49], [50-64], [65-79], [80+]\Big\}. \tag{S71}$$

Posterior samples were recorded in the 18 age bands used in the model ($[0-4]$, $[5-9]$, $\ldots$, $[85+]$) and then aggregated to the stratification $\mathcal{D}$ using

$$\begin{aligned} R_{m,t,d} &= \sum_{a \in d} \frac{c^*_{m,t,a}}{\sum_{k \in d} c^*_{m,t,k}} R_{m,t,a}, \\ c_{m,t,d} &= \sum_{a \in d} c_{m,t,a}, \\ d_{m,t,d} &= \sum_{a \in d} d_{m,t,a}, \end{aligned} \tag{S72}$$

where $c^*_{m,t,a}$ is the number of infectious individuals in location m and time t that is in age band a defined in (S75), $R_{m,t,a}$ is defined in (S23), $c_{m,t,a}$ is defined in (S25) and $d_{m,t,a}$ is defined in (S8).

Estimated cumulated COVID-19 attack rates by age and over time. We calculate the percentage of the population in m and in age band d that has been infected up to day t through

$$A_{m,t,d} = \frac{\sum_{s=1}^{t} c_{m,s,d}}{N_{m,d}}, \tag{S73}$$

where $N_{m,d}$ is the number of individuals in location m and age band d, and $c_{m,s,d}$ is defined in (S72). We also refer to (S73) as the age-specific cumulative attack rate. Similarly, we calculate the percentage of the population in m that has been infected up to day t through

$$A_{m,t} = \frac{\sum_d \sum_{s=1}^{t} c_{m,s,d}}{\sum_d N_{m,d}} = \sum_d \frac{N_{m,d}}{N_m} A_{m,t,d}, \tag{S74}$$

where N_m is the number of individuals in location m. We also refer to (S74) as the cumulative attack rate.

Estimated number of infectious individuals by age and over time. The effective number of infectious individuals c^* in location m and age band d on day t is calculated by weighing how infectious a previously infected individual is on day t,

$$c^*_{m,t,d} = \sum_{s=1}^{t-1} c_{m,s,d}\, g(t-s), \tag{S75}$$

where g appears in (S25). Similarly, the effective number of infectious individuals c^* in location m on day t is calculated by

$$c^*_{m,t} = \sum_d \sum_{s=1}^{t-1} c_{m,s,d}\, g(t-s) = \sum_{s=1}^{t-1} c_{m,s}\, g(t-s). \tag{S76}$$

Estimated time-varying reproduction number of COVID-19 over time. The overall time-varying reproduction number on day t in location m is given by

$$R_{m,t} = c_{m,t}/c^*_{m,t} \tag{S77}$$

where $c_{m,t}$ is the number of new cases on day t in location m, and $c^*_{m,t}$ is the number of infectious individuals on day t in location m [81]. Using the identity

$$\begin{aligned}
\sum_a R_{m,t,a} c^*_{m,t,a} &= \sum_a \sum_{a'} s_{m,t,a'} \rho_{a'} \mathbf{C}_{m,t,a,a'} c^*_{m,t,a} \\
&= \sum_{a'} \sum_a s_{m,t,a'} \rho_{a'} \mathbf{C}_{m,t,a,a'} c^*_{m,t,a} \\
&= \sum_{a'} c_{m,t,a'} \\
&= c_{m,t},
\end{aligned} \tag{S78}$$

Equation (S77) can be re-arranged to

$$R_{m,t} = \sum_a c^*_{m,t,a}/c^*_{m,t} R_{m,t,a}, \tag{S79}$$

where $R_{m,t,a}$ is defined in (S23).

Estimated age-specific SARS-CoV-2 transmission flows. Following on from Equation (S25), the transmission flows from age group a to age group a' at time t in location m are,

$$F_{m,t,a,a'} = s_{m,t,a'}\ \rho_{a'}\ \mathbf{C}_{m,t,a,a'} \left(\sum_{s=1}^{t-1} c_{m,s,a}\, g(t-s) \right), \tag{S80}$$

where $s_{m,t,a'}$ is defined in (S24), $\rho_{a,a'}$ is defined in (S22), and $\mathbf{C}_{m,t,a,a'}$ is defined in (S26). In terms of the age bands reported in the main text, the transmission flows by aggregated age groups are

$$F_{m,t,d,d'} = \sum_{a \in d, a' \in d'} F_{m,t,a,a'}. \tag{S81}$$

Estimated contribution of age groups to SARS-CoV-2 transmission. Following on from Equation (S80), the age-specific contribution of infections from age band a in location m on day t is

$$S_{m,t,a} = \left(\sum_{a'} F_{m,t,a,a'} \right) \Big/ \left(\sum_{a} \sum_{a'} F_{m,t,a,a'} \right). \tag{S82}$$

The age-specific contribution of infections are proportions, such that $\sum_a S_{m,t,a} = 1$ for all a. In terms of the age bands reported in the main text, the aggregated contribution of infections in age band d in location m on day t are equal to

$$S_{m,t,d} = \left(\sum_{d'} F_{m,t,d,d'} \right) \Big/ \left(\sum_{d} \sum_{d'} F_{m,t,d,d'} \right). \tag{S83}$$

National averages. Several quantities are reported at the national level by age,

$$R_{t,d} = \sum_m \frac{c^*_{m,t,d}}{\sum_l c^*_{l,t,d}} R_{m,t,d}, \tag{S84}$$

$$c_{t,d} = \sum_m c_{m,t,d}, \tag{S85}$$

$$d_{t,d} = \sum_m d_{m,t,d}, \tag{S86}$$

where $c^*_{m,t,d}$ is the number of infectious individuals at time t in location m and age band d, defined in (S75), and $R_{m,t,d}$, $c_{m,t,d}$ and $d_{m,t,a}$ are defined in (S72). Finally, for reporting at the national level regardless of age, we calculated

$$R_t = \sum_m \sum_{d \in \mathcal{D}} \frac{c^*_{m,t,d}}{\sum_l \sum_{k \in \mathcal{D}} c^*_{l,t,k}} R_{m,t,d}, \tag{S87}$$

$$c_t = \sum_d c_{t,d}, \tag{S88}$$

$$d_t = \sum_d d_{t,d}. \tag{S89}$$

S3.7 Counterfactual scenarios

Time period of counterfactual scenarios. Counterfactual scenarios on the likely epidemic outcomes were investigated retrospectively, starting at a day in the past and considering counterfactual simulations until the last observation day, October 29, 2020. This strategy allowed us to investigate what would have happened if one of the model parameters had been different, while keeping all other model parameters at their best fit values that best reproduce epidemic trajectories as of October 29, 2020. We focused on the impact of alternative, counterfactual school re-opening scenarios between August 24, 2020 and October 29, 2020, which corresponds to the last day with death data in the analysis.

Counterfactual school closure scenario. In this counterfactual scenario, we assumed that kindergartens, and elementary, middle and high schools would have remained closed between August 24, 2020 and October 29, 2020 in all states and metropolitan areas evaluated. This scenario was implemented via Equation (S35), by setting the school re-opening time index $t_m^{\text{school-reopen}}$ to past the last observation day in all states, October 30, 2020. Output quantities were then generated from the model with all other parameters sampled from their inferred joint posterior distribution.

Counterfactual school re-opening scenario. In this counterfactual scenario, we assumed that schools reopened on August 24, 2020 in all locations, and that there would not have been a reduction in disease-relevant contacts from and to school-aged children. This scenario was implemented via Equation (S35), by setting the school re-opening time index $t_m^{\text{school-reopen}}$ to August 24, 2020 in all states, and by setting $\eta^{\text{children}} = 1$ and $\gamma = 1$. Output quantities were then generated from the model with all other parameters sampled from their inferred joint posterior distribution.

Age stratification for school re-opening scenarios. To quantify the impact of the school re-opening scenarios, we used the age bands

$$\tilde{d} \in \tilde{\mathcal{D}} = \Big\{[0-9], [10-18], [19-34], [35-49], [50-64], [65-79], [80+]\Big\}. \tag{S90}$$

We introduce the superscript x to denote the various counterfactual scenarios. Then, in the counterfactual scenarios, time-varying reproduction numbers were calculated through

$$R^x_{m,t,\tilde{d}} = \begin{cases} \dfrac{c^*_{m,t,[10-14]} R^x_{m,t,[10-14]} + \frac{4}{5} c^*_{m,t,[15-19]} R^x_{m,t,[15-19]}}{c^*_{m,t,[10-14]} + \frac{4}{5} c^*_{m,t,[15-19]}} & \text{if } \tilde{d} = [10-18] \\ \dfrac{\frac{1}{5} c^*_{m,t,[15-19]} R^x_{m,t,[15-19]} + \sum_{a \in \{[20-24],[25-29],[30-34]\}} c^*_{m,t,a} R^x_{m,t,a}}{\frac{1}{5} c^*_{m,t,[15-19]} + \sum_{k \in \{[20-24],[25-29],[30-34]\}} c^*_{m,t,k}} & \text{if } \tilde{d} = [19-34] \\ \displaystyle\sum_{a \in \tilde{d}} \frac{c^*_{m,t,a}}{\sum_{k \in d} c^*_{m,t,k}} R^x_{m,t,a} & \text{if } \tilde{d} < 10 \text{ or } \tilde{d} > 34. \end{cases} \tag{S91}$$

The number of daily new cases were calculated through

$$c^x_{m,t,\tilde{d}} = \begin{cases} c^x_{m,t,[10-14]} + \dfrac{4}{5} c^x_{m,t,[15-19]} & \text{if } \tilde{d} = [10-18] \\ \dfrac{1}{5} c^x_{m,t,[15-19]} + \displaystyle\sum_{a \in \{[20-24],[25-29],[30-34]\}} c^x_{m,t,a} & \text{if } \tilde{d} = [19-34] \\ \displaystyle\sum_{a \in \tilde{d}} c^x_{m,t,a} & \text{if } \tilde{d} < 10 \text{ or } \tilde{d} > 34. \end{cases} \tag{S92}$$

The number of daily deaths were calculated through

$$d^x_{m,t,\tilde{d}} = \begin{cases} d^x_{m,t,[10-14]} + \frac{4}{5} d^x_{m,t,[15-19]} & \text{if } \tilde{d} = [10-18] \\ \frac{1}{5} d^x_{m,t,[15-19]} + \sum_{a \in \{[20-24],[25-29],[30-34]\}} d^x_{m,t,a} & \text{if } \tilde{d} = [19-34] \\ \sum_{a \in \tilde{d}} d^x_{m,t,a} & \text{if } \tilde{d} < 10 \text{ or, } \tilde{d} > 34. \end{cases} \quad \text{(S93)}$$

The transmission flows of age group $\tilde{d}$ on day t in location m and scenario x were calculated through

$$F^x_{m,t,\tilde{d}} = \begin{cases} \frac{9}{10} F^x_{m,t,[10-19]} & \text{if } \tilde{d} = [10-18] \\ \frac{1}{10} F^x_{m,t,[10-19]} + F^x_{m,t,[20-34]} & \text{if } \tilde{d} = [19-34] \\ F^x_{m,t,d} & \text{if } \tilde{d} < 10 \text{ or } \tilde{d} > 34. \end{cases} \quad \text{(S94)}$$

Based on Equations (S91-S94), the excess cumulative number of cases in the observed data versus the counterfactual continued school closure scenario during the time period of the counterfactual was calculated as

$$c^{\text{excess}}_{m,\tilde{d}} = \Big(\sum_{t=t^{\text{school-reopen}}_m}^{t^{\text{end}}_m} c^{\text{observed}}_{m,t,\tilde{d}} \Big) - \Big(\sum_{t=t^{\text{school-reopen}}_m}^{t^{\text{end}}_m} c^{\text{closure}}_{m,t,\tilde{d}} \Big). \quad \text{(S95)}$$

The percent increase in cumulated cases in the observed data versus the continued school closure scenario during the time period of the counterfactual was calculated as

$$c^{\text{pc-increase}}_{m,\tilde{d}} = \Big(\sum_{t=t^{\text{school-reopen}}_m}^{t^{\text{end}}_m} c^{\text{observed}}_{m,t,\tilde{d}} \Big) \Big/ \Big(\sum_{t=t^{\text{school-reopen}}_m}^{t^{\text{end}}_m} c^{\text{closure}}_{m,t,\tilde{d}} \Big) - 1. \quad \text{(S96)}$$

Predicted excess deaths and percent increases in deaths were calculated analogously. Comparisons between the counterfactual school re-opening scenario as if non-pharmaceutical interventions would have had no effect and/or children and teens are as infectious as adults versus the observed data were also done analogously.

S4 Comparison of model outputs to estimated contact intensities during the pandemic

The SARS-CoV-2 transmission model presented in Section S3.1 makes detailed predictions on the time evolution of age-specific contact patterns during the pandemic. As a form of external model validation, we here compare the model predictions against data from contact survey studies.

In the US, the Berkeley Interpersonal Contact Study (BICS) was designed to measure the effects of social distancing on contact patterns during the pandemic, and began in spring 2020 [82]. Their study included adults aged 18+ and wave 0 was conducted between March 22 to April 08, 2020. In this wave, approximately half the study participants were from five cities (New York, San Francisco Bay Area, Atlanta, Phoenix, Boston) with the rest from around the rest of the US. In their initial analyses, the study authors found that individuals had a mean of 2.7 conversational contacts with similar IQR when compared to the study of Jarvis et al. [73] in the UK: 85% of respondents reported four or fewer contacts. Despite wide confidence intervals, these figures indicate substantial reductions in the overall number of contacts in the early phase of the pandemic, and early after lockdown or stay at home orders were issued.

We compared the estimates from the two contact surveys to the average number of contacts at the midpoint of the wave 0 period of the BICS study, March 28, 2020 (Table S12). To match the study sample of the BICS study, we report estimates for two metropolitan areas included in the model analysis (New York City and District of Columbia), and an overall estimate for the US obtained by averaging across all states evaluated, New York City, and the District of Columbia. Overall, the COVID-19 contact and infection model estimates similar strong reductions in the number of daily contacts, with a probability of one that overall, the average number of daily contacts by individuals of all ages was at most four.

Table S12: Estimated number of contacts on March 28, 2020 (midpoint of BICS wave0 study). Posterior median and 95% credible intervals in brackets. We include a weighted average across the US and two cities which were included in the BICS study.

	Number of daily contacts [95% credible intervals]	Posterior probability of at most 4 daily contacts
District of Columbia	2.69 [1.92 - 3.74]	100%
New York City	2.23 [1.8 - 2.72]	100%
United States	2.87 [2.75 - 2.99]	100%

We also compared the age breakdown of daily number of conversational contacts from the BICS study with our model estimates for New York City, District of Columbia and a national average. Fig. S32 indicates good agreement between the estimates of the BICS study and model fits.

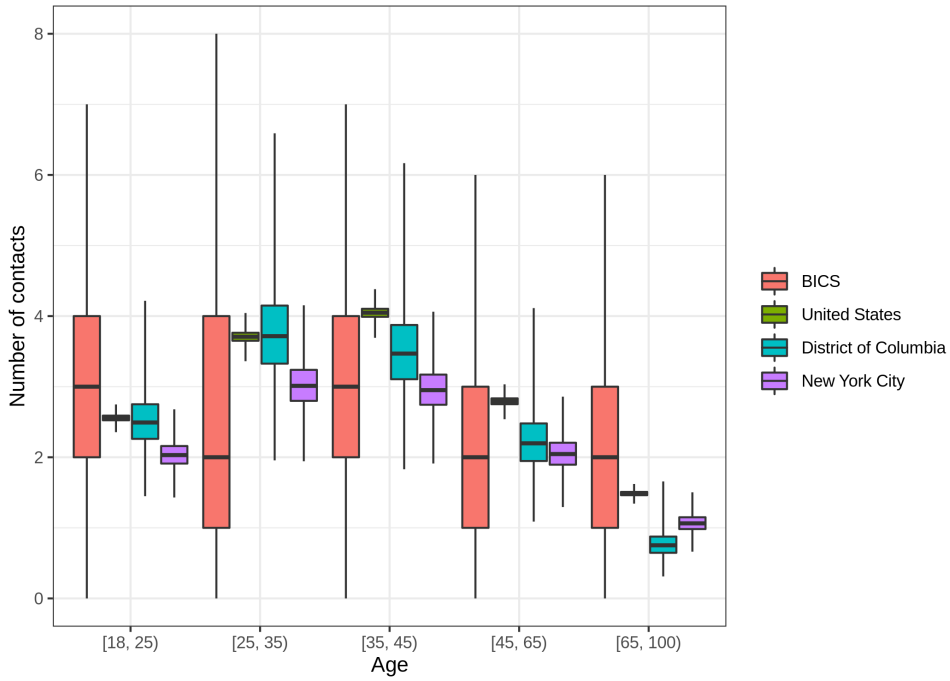

Figure S32: Estimated daily number of contacts per age band on March 28, 2020 (midpoint of BICS wave0 study).

S5 Comparison of model outputs to seroprevalence estimates

To further assess model fit, we reviewed data from several large-scale COVID-19 seroprevalence surveys in the US, and qualitatively compared the sero-prevalence estimates from the antibody surveys to the estimates under the contact and infection model at location.

We included 32 COVID-19 antibody surveys from across the US in this comparison (Table S13). 31 studies were conducted by the U.S. Centers for Disease Control & Prevention (CDC) in 7 locations, Connecticut, Florida, Louisiana, Minnesota, Missouri, New York City, Utah, and Washington. Multiple rounds of seroprevalence surveys were done in each location, except Louisiana where one seroprevalence survey was performed. The surveys included individuals who had blood specimens tested for reasons unrelated to COVID-19 [79], and thus the study samples may not be representative of the underlying populations. For instance, the CDC compared the predicted number of total infections obtained under the COVID-19 sero-prevalence estimates to the number of reported cases, and found that in most locations, approximately one in ten cases were reported. However for the study in Connecticut, the ratio was one in six, and for the study in Missouri, the ratio was one in 24, suggesting that the study samples in these locations may not be representative. The final survey included in the comparison was also from New York City [83], and included participants recruited through flyers at the entrances of grocery stores. Individuals who are less likely to visit grocery stores may have lower infection risk (e.g. because of self-isolation) or higher infection risk (e.g. quarantine after infection), and estimates from this study may

also be subject to unknown biases.

Table S13: Characteristics of large-scale antibody studies used for the comparison. All dates are for the year 2020. Data were retrieved from the CDC dashboard [84].

Study	Round	Period	Number of participants
Connecticut	1	Apr 26 - May 3	1431
	2	May 21 - May 26	1800
	3	Jun 15 - Jun 17	1798
	4	Jul 7 - Jul 6	1802
	5	Jul 27 - Jul 27	1799
Louisiana	1	Apr 1 - Apr 8	1184
Minnesota	1	Apr 30 - May 12	860
	2	May 25 - Jun 7	1323
	3	Jun 15 - Jun 27	1667
	4	Jul 6 - Jul 18	1677
	5	Jul 27 - Aug 8	1588
Missouri	1	Apr 20 - Apr 26	1882
	2	May 25 - May 30	1831
	3	Jun 15 - Jun 20	1850
	4	Jul 5 - Jul 9	1914
	5	Jul 27 - Jul 30	1931
New York City Metro Area	1	Mar 23 - Apr 1	2482
	2	Apr 6 - Apr 16	1618
	3	Apr 27 - May 6	1116
	4	Jun 15 - Jun 21	1581
	5	Jul 7 - Jul 11	1602
	6	Jul 27 - Jul 30	1547
Philadelphia Metro Area	1	Apr 13 - Apr 25	824
	2	May 26 - May 30	1743
	3	Jun 14 - Jun 20	1694
	4	Jul 6 - Jul 11	1751
	5	Jul 27 - Aug 8	1730
San Francisco Bay Area	1	Apr 23 - Apr 27	1224
	2	May 19 - May 27	1539
	3	Jul 20 - Jul 23	1223
South Florida	1	Apr 6 - Apr 10	1742
	2	Apr 20 - Apr 24	1280
	3	Jun 19 - Jun 17	1790
	4	Jul 20 - Jul 23	1721
Utah	1	Apr 20 - May 3	1132
	2	May 25 - Jun 5	1940
	3	Jun 25 - Jun 27	1976
	4	Jul 6 - Jul 15	1824
	5	Jul 27 - Aug 6	1906
Western Washington Region	1	Mar 23 - Apr 1	3264
	2	Apr 27 - May 11	1719
	3	Jun 15 - Jun 20	1803
	4	Jul 6 - Jul 7	1797
	5	Jul 27 - Jul 31	1718

In all studies, IgM and IgG enzyme-linked immunosorbent assays (ELISA) were used to test for COVID-19 antibodies. Common limitations of these tests are that infected individuals with antibodies may test negative (false negatives), uninfected individuals without antibodies may test positive (false positives), that infected individuals may not yet have developed antibodies (antibody eclipse phase), and that infected individuals may have already lost antibodies (sero-reversion). The above studies adjusted sero-prevalence estimates for false positive and false negative rates, however re-analyses of manufacturer sensitivity and specificity figures suggest that these numbers may have to be considered with caution [5]. To account for the antibody eclipse phase, we calculated as part of the infection model the number of

expected infected individuals with antibodies. Specifically, COVID-19 symptoms are estimated to develop on average 6 days after infection (estimated range 2 to 14 days) [85] and individuals are estimated to develop IgG antibodies on average 14 days after symptom onset (estimated range 7 to 21 days) [86, 87]. Based on these estimates, we specified the infection-to-onset-of-symptoms distribution and the onset-to-antibody distribution as the sum of both components through

$$k(s) = \text{Gamma}(s; 5.1, 0.86) + \text{Normal}(s; 14, 3.57) \tag{S97}$$

where s is in continuous time. We then express the probability that a person in location m and age band a develops antibodies on day s after SARS-CoV-2 infection as

$$k_s = \int_{s-0.5}^{s+0.5} k(u)du = \int_{s-0.5}^{s+0.5} k(u)du \quad \forall s = 2, 3, \ldots, \tag{S98}$$

and $k_s = \int_0^{1.5} k(u)du$ for $s = 1$. Using (S98), the expected number of infected individuals that develop COVID-19 antibodies on day t in age band a in location m is

$$b_{m,t,a} = \sum_{s=1}^{t-1} c_{m,s,a}\, k_{t-s}, \tag{S99}$$

where $c_{m,s,a}$ is the expected number of new cases on day s in age band a in location m, (S25). In the model seroreversion was not considered, and the expected proportion of individuals with COVID-19 antibodies on day t in location m was calculated as

$$s_{m,t} = \Big(\sum_a \sum_{s=1}^{t} b_{m,s,a} \Big) / N_m, \tag{S100}$$

where N_m is the number of individuals in location m. The day of comparison was set to the last day of the study period. For the New York City study [83], the Utah study, the second round of the Florida and Minnesota studies, and the fourth round of the Washington study, individuals up to age 18 were excluded from calculation of the sero-prevalence estimate (S100), because of small sample sizes in the surveys.

Fig. S33 compares the expected proportion of individuals with COVID-19 antibodies (S100) to study estimates. For Connecticut, the model estimates higher seroprevalence levels than the CDC study. However under the estimates of the CDC study, the ratio of expected to observed cases was unusually low at 6:1 or lower across the study rounds, suggesting that seroprevalence was likely underestimated in that study by a factor of two. An alternative explanation is that the model does not account for sustained spatial importation of SARS-Cov-2 infections such as from New York City, and may have overestimated local transmission dynamics. For Florida, survey samples were collected in South Florida, which experienced higher numbers of reported cases and contributed disproportionately towards total deaths within the state. This suggests that survey estimates likely overstated seroprevalence compared to the state as a whole, and the implications on our comparison are unclear. For the round 1 study in Missouri, we note

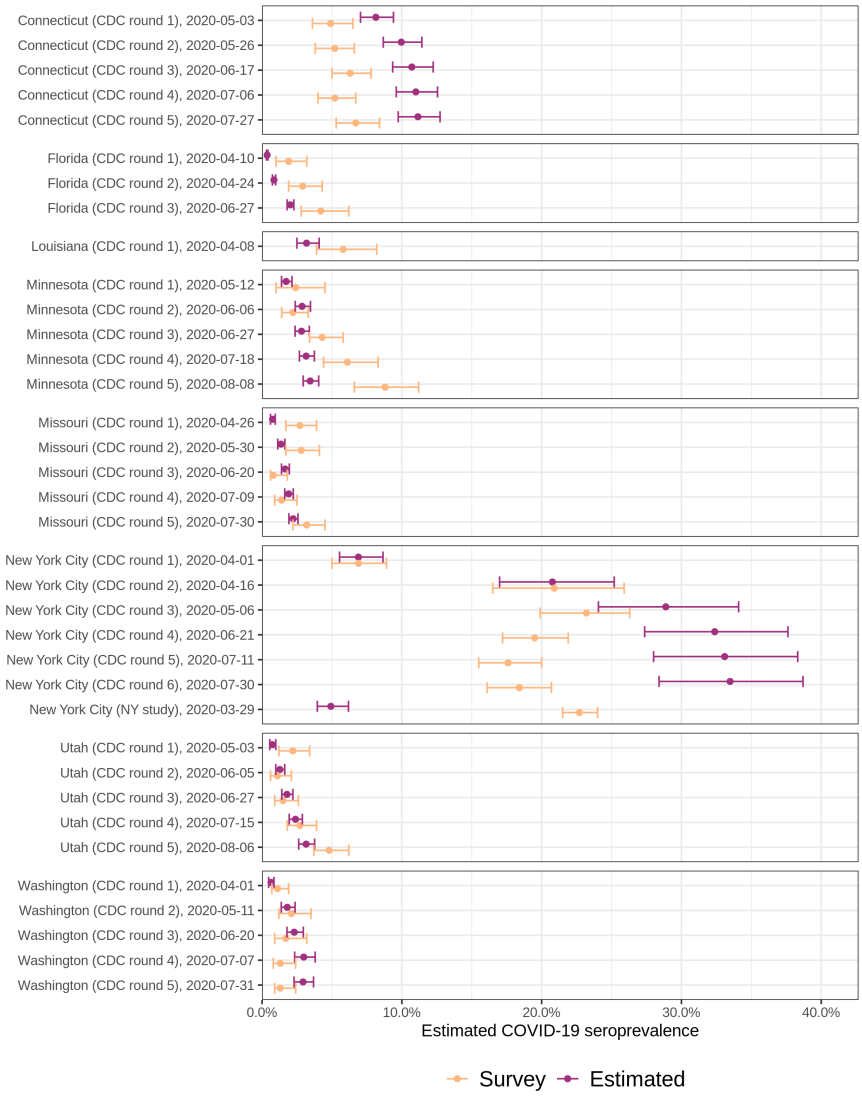

Figure S33: Comparison between estimates of COVID-19 seroprevalence under the contact and infection model with those from large-scale antibody studies. Shown are posterior medians and 95% credible intervals for model output, and estimates as reported from the antibody studies, for the dates reported by the studies.

the ratio of expected to observed cases was unusually high at 23:1, suggesting that seroprevalence was likely overestimated in the study by a factor of two. In contrast, low ratios of 3:1 of expected to observed cases in the third and fourth round suggest underestimation of seroprevalence in these rounds. For the New York metropolitan area, the catchment area increased from round 1 to round 2 to include Long Island, suggesting that the survey estimates could understate seroprevalence compared to New York City in early May. The survey estimates decreased from rounds 2 to 4. Seroreversion was not considered in the model, and so a poorer fit to actual seroprevalence data at later time points is expected. For Utah,

the round 2 point estimate is significantly lower than that of round 1, though the 2:1 ratio of expected to observed cases in rounds 2 to 4, may indicate underestimation by a factor of 5. For Washington, survey samples were collected in the Western region, which also experienced higher case and death numbers than the Eastern part of Washington state, suggesting that survey estimates could have overstated state-level seroprevalence. The second New York City study [83] found considerably higher seroprevalence estimates at a time point before the first CDC study in New York City. Our model estimates appear to be more in line with the sero-prevalence estimates of the CDC studies in New York City. In the context of these potential caveats, we find that the model fits are qualitatively in good agreement with available seroprevalence data. The corresponding cumulative attack rates estimates are presented in Table S6.

DOI: https://doi.org/10.25561/82551

S6 Sensitivity analyses

S6.1 Alternative assumptions on age-specific infection fatality ratios

The contact-and-infection model is sensitive to the underlying infection fatality rates (IFR), as any model that infers disease dynamics from COVID-19 attributable deaths [56, 88]. The central analysis uses an IFR prior that is centered on the version 7 meta-analysis estimates of Levin and colleagues [89]. The contact and infection model is sensitive to the assumed IFR prior, as any model that infers disease dynamics from COVID-19 attributable deaths [56]. In sensitivity analyses, we considered an alternative IFR prior density centered on the version 5 meta-analysis estimates of Levin and colleagues [89], which were lower for younger age bands and higher for older age bands (Figure S34).

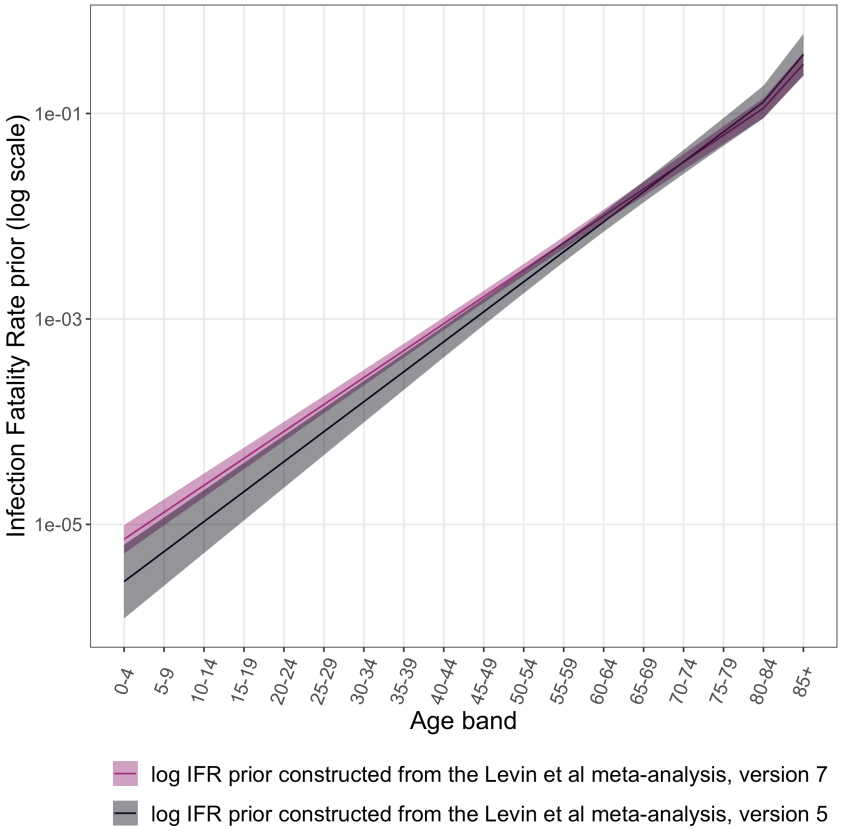

Figure S34: Comparison of age-specific IFR estimates used in the central analysis and the sensitivity analysis. Mean and 95% uncertainty ranges of age-specific IFR estimates from version 5 and version 7 of the meta-analysis of [89]. Version 7 was used in the central analysis, and version 5 in the sensitivity analysis..

Figure S35 compares the cumulative attack rates in each location that were estimated under the central model, and the alternative model that uses the version 5 meta-analysis IFR estimates. In the sensitivity analysis, estimated cumulative attack rates were in some locations considerably higher among

individuals aged < 70 than in the central analysis. Figure S36 compares the seroprevalence estimates under both models to the estimates of the seroprevalence studies described in Section S5. The seroprevalence estimates in the central analysis showed smaller differences relative to the estimates of the CDC seroprevalence studies, when compared to the estimates in the sensitivity analysis.

Figure S37 compares estimates of age-specific reproduction numbers and the contribution of age groups to onward spread under the central model, and the alternative model that uses the version 5 meta-analysis IFR estimates. Both models made very similar inferences on age-specific disease spread. This suggests that the estimated scale of COVID-19 epidemics depends on the assumed IFR, resulting in >5% differences in estimated cumulative attack rates for less than a one order of magnitude change in IFR estimates among young age groups. However differences in the estimated scale of the epidemics had no significant impact on estimated reproduction numbers, and the estimated contribution of age groups to SARS-Cov-2 infection.

DOI: https://doi.org/10.25561/82551

Figure S35: Age-specific cumulative attack rate estimates under the central model and under the alternative model using an IFR prior density centered at alternative meta-analysis estimates. Dots and error bars indicate the posterior median estimate and 95% credible intervals in cumulative attack rates as of August 23, 2020. Central model is in purple and alternative model is in black.

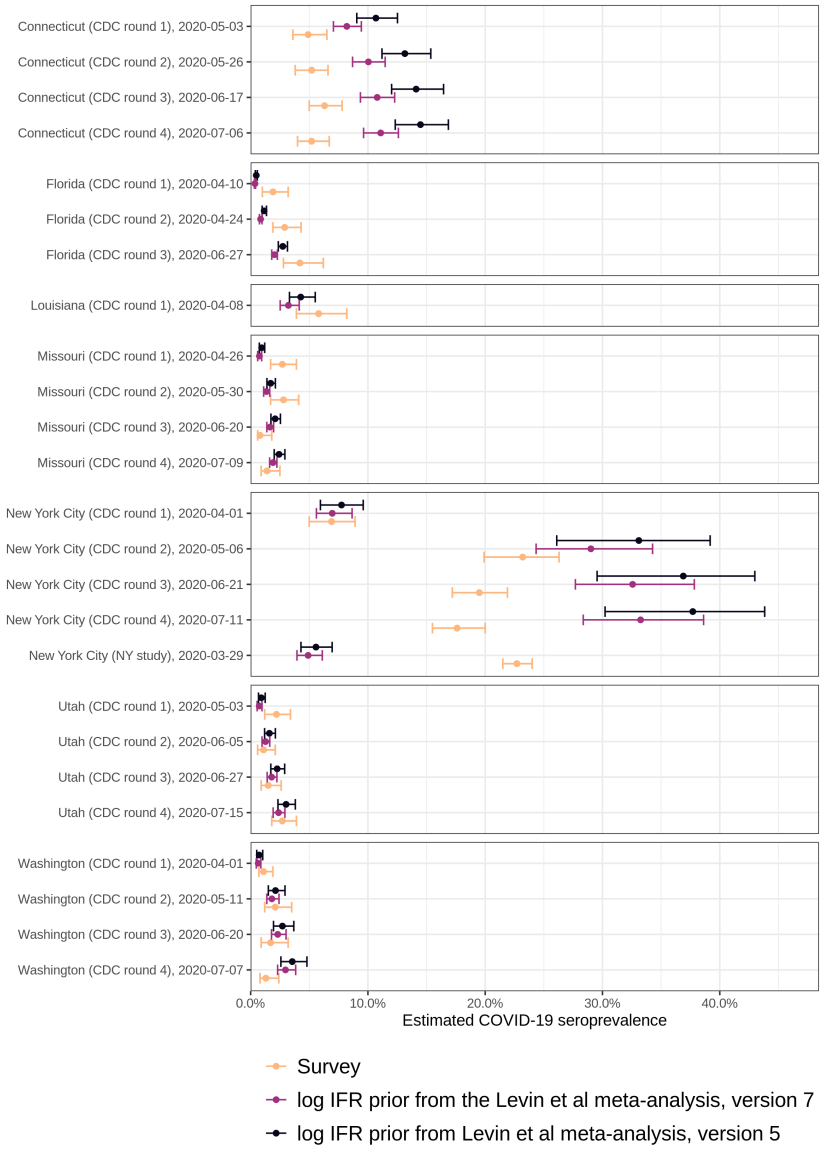

Figure S36: Comparison of seroprevalence estimates from the central model and the alternative model using an IFR prior density centered at alternative meta-analysis estimates. Shown are posterior medians and 95% credible intervals for the model estimates on the midpoint of the observation periods of the seroprevalence studies, against estimates from the seroprevalence surveys (see Section S5).

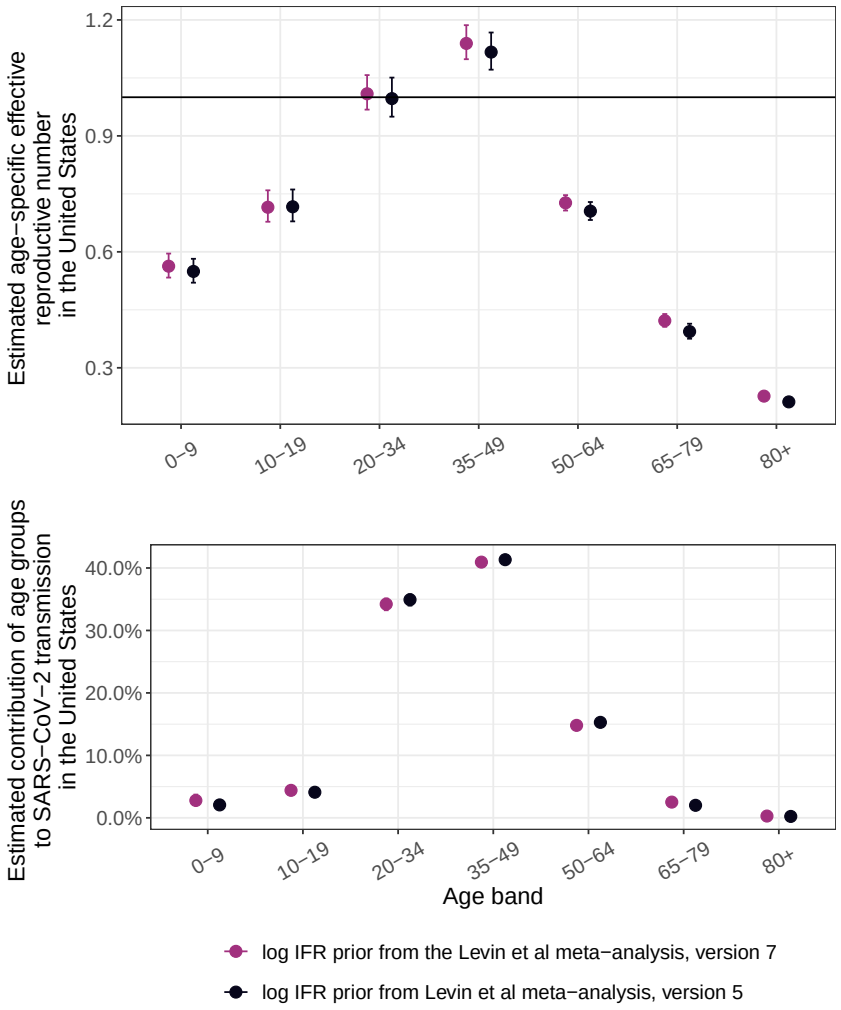

Figure S37: Age-specific weekly reproduction numbers and contribution of age groups to onward spread under the central model and under the alternative model using an IFR prior density centered at alternative meta-analysis estimates. (Top) Estimated weekly age-specific reproduction numbers for the week August 17, 2020 - August 23, 2020 under the central model (purple) and the alternative model (black). Dots and error bars indicate the posterior median estimate and 95% credible intervals. (Bottom) Estimated cumulative contribution of age groups to onward spread as of August 17, 2020.

S6.2 Alternative assumptions on contact intensities from and to children aged 0-19 during periods of school closure

The cell-phone derived population-level mobility data used in this study were only available for individuals aged $18+$. We rely on limited data from two contact surveys performed in the United Kingdom and China [73, 54] to characterise contact patterns from and to younger individuals during the pandemic (as described in Section S3.2). In the central analysis, the $4 \times 4 + (18-4) \times 4 + 4 \times (18-4) = 128$ contact intensities from or to children and teens aged 0-19 were set to the corresponding, average of the age-specific contact intensities during lockdown that were observed across location in [54]; see also Equation (S35). In sensitivity analyses, we explored the impact of lower or higher contact intensities from or to children and teens aged 0-19 during periods of school closures. We approached this by re-formulating (S35) to the following form,

$$\mathbf{C}_{m,t,a,a'} = \begin{cases} \mathbf{C}_{m,a,a'} & \text{if } t < t_m^{\text{school-close}} \\ \tau \mathbf{C}_{a,a'}^{lckdwn-0-19} & \text{if } t \in [t_m^{\text{school-close}}, t_m^{\text{school-reopen}} - 1] \\ \mathbf{C}_{m,a,a'}^{\text{reopen-0-19}} & \text{if } t \geq t_m^{\text{school-reopen}} \end{cases} \tag{S101}$$

where $a \in \{[0-4], [5-9], [10-14], [15-19]\}$ or a' is one of the 5-year age bands of the infection-and-contact model, $t_m^{\text{school-close}}$ is the time index corresponding to schools closure in location m, $t_m^{\text{school-open}}$ is the time index corresponding to schools re-opening in location m, $\mathbf{C}_{m,a,a'}$ are the baseline pre-COVID-19 contact intensities described in location m in Section S3.2.2, $\mathbf{C}^{lckdwn-0-19}$ are the average contact intensities derived from [54], and τ is a new scaling factor that we introduce for the purpose of sensitivity analyses.

To gauge a range of τ values, we first calculated the contact intensity ratios between the city-level contact matrices in [54] with the contact intensities $\mathbf{C}^{lckdwn-0-19}$ that were used in the central analysis. The maximum contact intensity ratio was 2.00 and the minimum was 0.15. Using data from the UK post lockdown contact survey of Jarvis and colleagues [73], we also computed the mean contact intensities from individuals aged $18+$ with children aged $0-4$ and children and teens age $5-17$. We repeated calculations for the average post-lock down contact matrix $\mathbf{C}^{lckdwn-0-19}$ of Jarvis and colleagues [73]. The minimum and maximum ratio in the corresponding contact intensities were 1.79 and 2.22. We thus performed two sensitivity analyses using $\tau = 0.5$ and 2, subject to the constraint that the resulting contact intensities during lockdown were not larger than those prepandemic contact intensities $\mathbf{C}_{m,a,a'}$. Figure S38 compares the resulting contact intensities from and to children and teens during periods of school closure.

Then, we re-fitted the contact-and-infection model. Figure S39 compares estimates of age-specific reproduction numbers, and the contribution of age groups to onward spread under the central and alternative models. The alternative model assumptions lead to considerable differences in estimated, age-specific reproduction numbers. For children aged $0-9$, the estimated reproduction numbers ranged from 0.30 [0.29, 0.32] to 0.83 [0.79, 0.88] as τ increased from 0.5 to 2 in the week August 17, 2020 - August 23, 2020. For teens aged 10-19, the estimated reproduction numbers ranged from 0.37 [0.35,

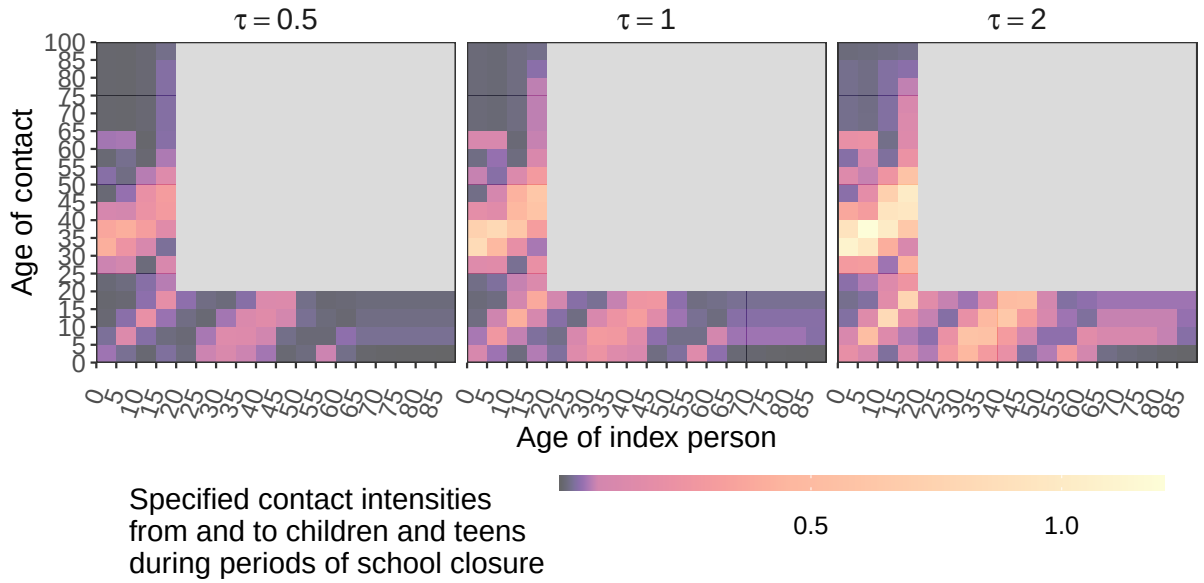

Figure S38: Comparison of contact intensities from and to children aged 0-19 during periods of school closures in the central and sensitivity analyses. Shown are contact intensities from and to children and teens during periods of school closure (on May 06, 2020) in California for different values of τ in Equation (S101). The value $\tau = 1$ corresponds to the central analysis. Parts of the time varying contact matrices that are not affected by this change in model assumptions are shown in grey.

0.39] to 1.28 [1.21, 1.36] as τ increased from 0.5 to 2. These differences also had a noticeable impact on the estimated contribution of children and teens to SARS-CoV-2 transmission. The estimated cumulative contribution to onward spread from children aged 0-9 as of August 17, 2020 increased from 1.78% [1.38%-2.19%] to 3.08% [2.38%-3.93%] as τ increased from 0.5 to 2. For teens aged 10-19, the estimated cumulative contribution to onward spread increased from 2.24% [1.88%-2.62%] to 10.89% [9.64%-12.37%] as τ increased from 0.5 to 2. Conversely, for young adults aged 20-34, the estimated cumulative contribution to onward spread decreased for all other age groups as τ increased from 0.5 to 2. This analyses indicate that reproduction numbers from teens aged 10-19 can in principle rise well above 1, and that teens can contribute substantially to onward infection, if their disease relevant contact intensities are assumed to be twice as high as in the central analysis. However when potential reductions in disease relevant contacts are estimated based on case and death data after school reopening, we find substantial positive effects, which render the $\tau = 2$ scenario unlikely.

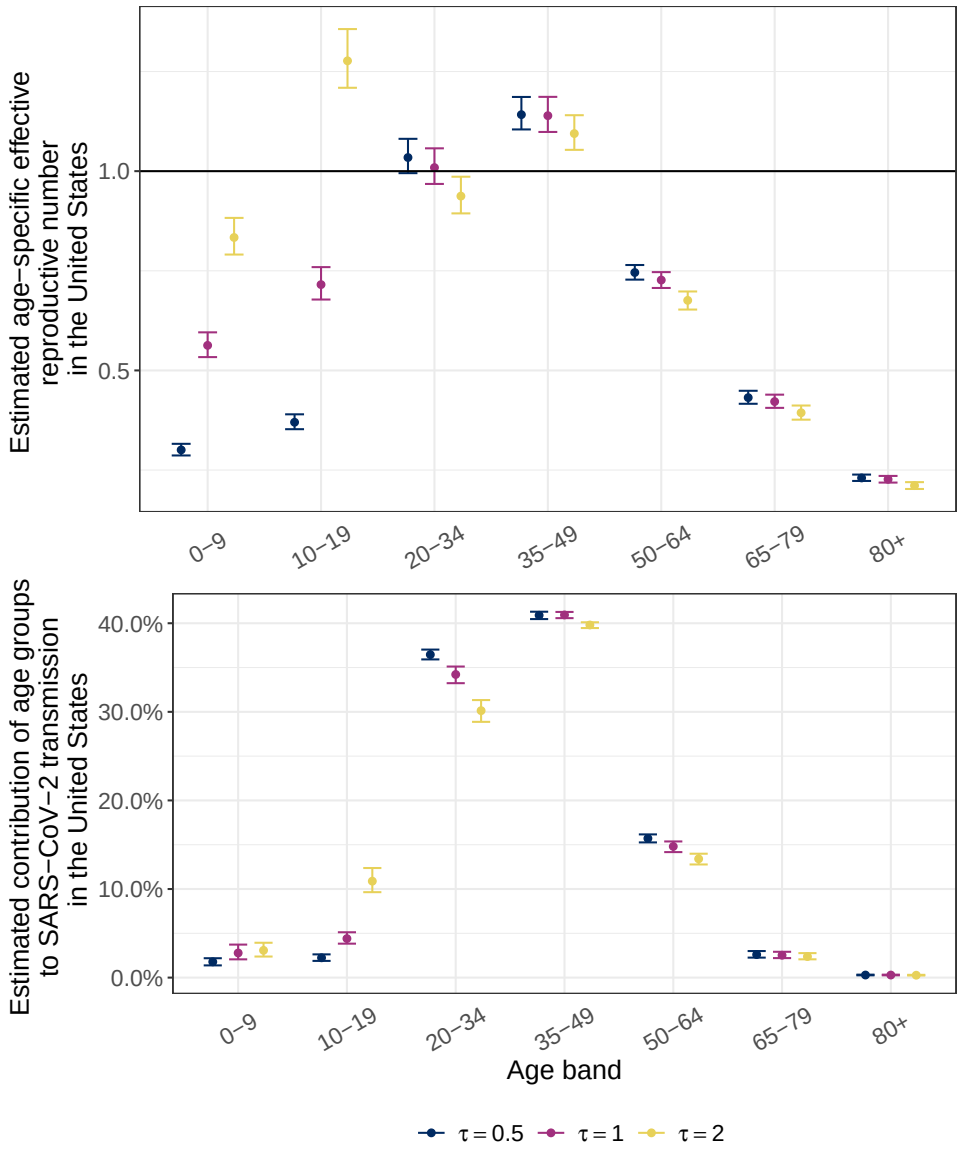

Figure S39: Age-specific weekly reproduction numbers and contribution of age groups to onward spread under the central model and under the alternative models using different assumption on contact intensities from and to children and teens aged 0-19 during periods of school closure. (**A**) Estimated age-specific reproduction numbers for the week August 17, 2020 to August 23, 2020 under the central model (purple) and the alternative models; see (S101). (**B**) Estimated cumulative contribution of age groups to onward spread as of August 17, 2020 under the central model (purple) and the alternative models. The value $\tau = 1$ corresponds to the central model. Dots and error bars indicate the posterior median estimate and 95% credible intervals.

S6.3 Alternative assumptions on the relative susceptibility parameters

An important feature of SARS-CoV-2 transmission is that susceptibility to SARS-CoV-2 infection increases with age [90, 91]. In the central analysis, the relative susceptibility parameters in (S51) are informed by the contact tracing study of Zhang and colleagues [54]. In the sensitivity analysis, we considered instead an alternative prior density on the relative susceptibility parameters based on the meta-analysis of Viner and colleagues [90]. We approached this by reformulating (S51) to the following form

$$\log \rho^S_{[0-9]} \sim \mathcal{N}(-0.6833129, 0.242431^2) \tag{S102a}$$

$$\log \rho^S_{[10-19]} \sim \mathcal{N}(-0.353706, 0.2245081^2) \tag{S102b}$$

$$\log \rho^S_{[65+]} \sim \mathcal{N}(0.3828, 0.1638^2), \tag{S102c}$$

where the hyperparameters were obtained by fitting a lognormal distribution to the reported 95% confidence intervals in [90] with the `lognorm` R package, version 0.1.6 [76]. The log susceptibility parameters for the age band $[20-64]$ were set to 0, so that ρ^S can be interpreted as the relative risk of SARS-CoV-2 infection among individuals aged 0-9, 10-19, $65+$ relative to individuals aged $20-64$. Considering the 18 age bands of the contact-and-infection model, the age-specific relative susceptibility parameters were set to

$$\log \rho^S_a = \begin{cases} \log \rho^S_{[0-9]} & \text{if } a \in [0-9] \\ \log \rho^S_{[10-19]} & \text{if } a \in [10-19] \\ \log \rho^S_{[20-64]} & \text{if } a \in [20-64] \\ \log \rho^S_{[65+]} & \text{if } a \in [65+]. \end{cases} \tag{S103}$$

in the sensitivity analysis. Thus, in the sensitivity analysis, the relative risk of SARS-Cov-2 infection among children and teens was higher than in the central analysis.

Figure S40 compares estimates of age-specific reproduction numbers, and the contribution of age groups to onward spread under the central model to those under the alternative model that uses relative susceptibility estimates of Viner et al. [90]. Both models made very similar inferences on age-specific disease spread. Figure S41 compares the cumulative attack rates estimated under the central model to those under the alternative model. Both models displayed similar estimates on age-specific SARS-CoV-2 burden.

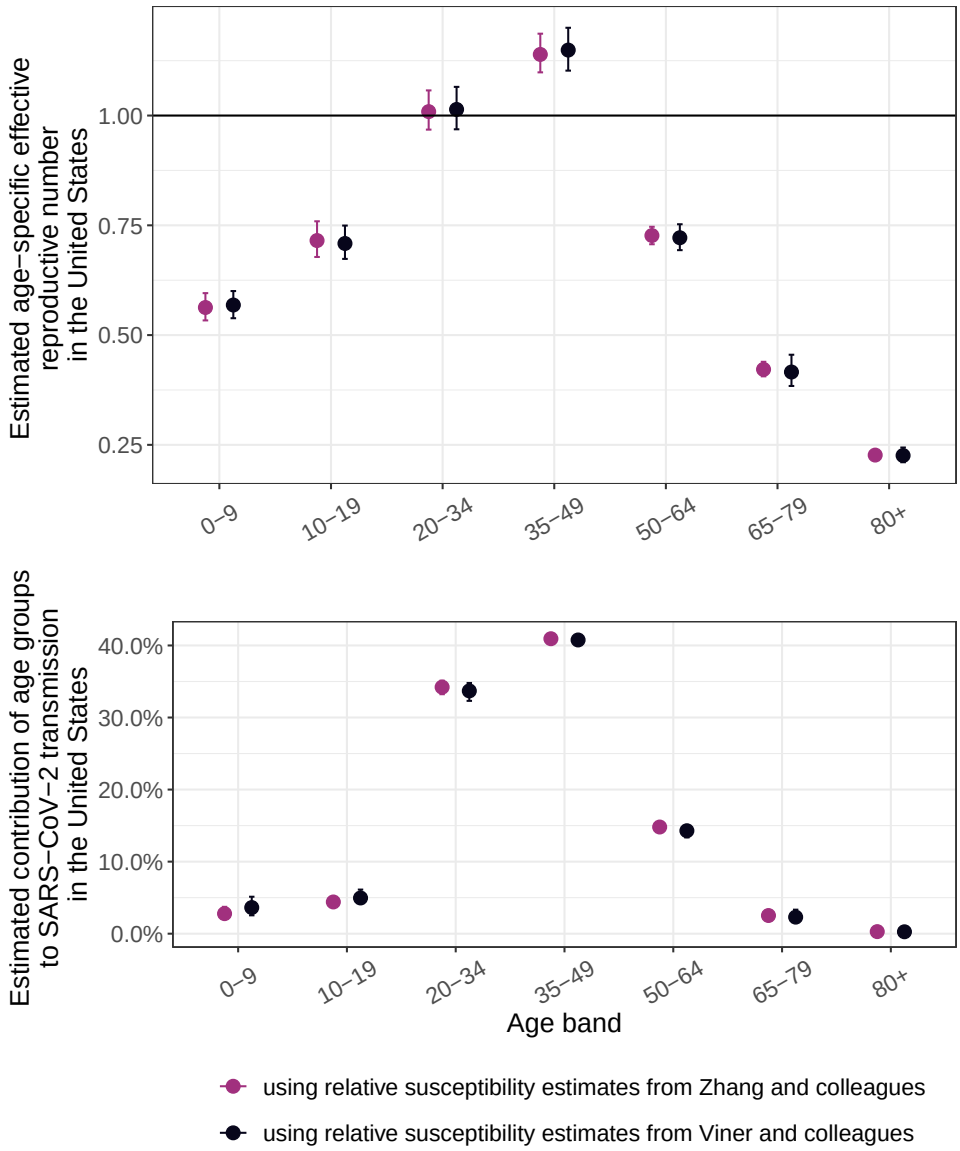

Figure S40: Age-specific weekly reproduction numbers and contribution of age groups to onward spread under the central model and under the alternative model that uses relative susceptibility estimates of Viner et al. [90] (Top) Estimated weekly age-specific reproduction numbers for the week August 17, 2020 to August 23, 2020 under the central model (purple) and the alternative model (black). (Bottom) Estimated cumulative contribution of age groups to onward spread as of August 17, 2020. Dots and error bars indicate posterior median estimates and 95% credible intervals.

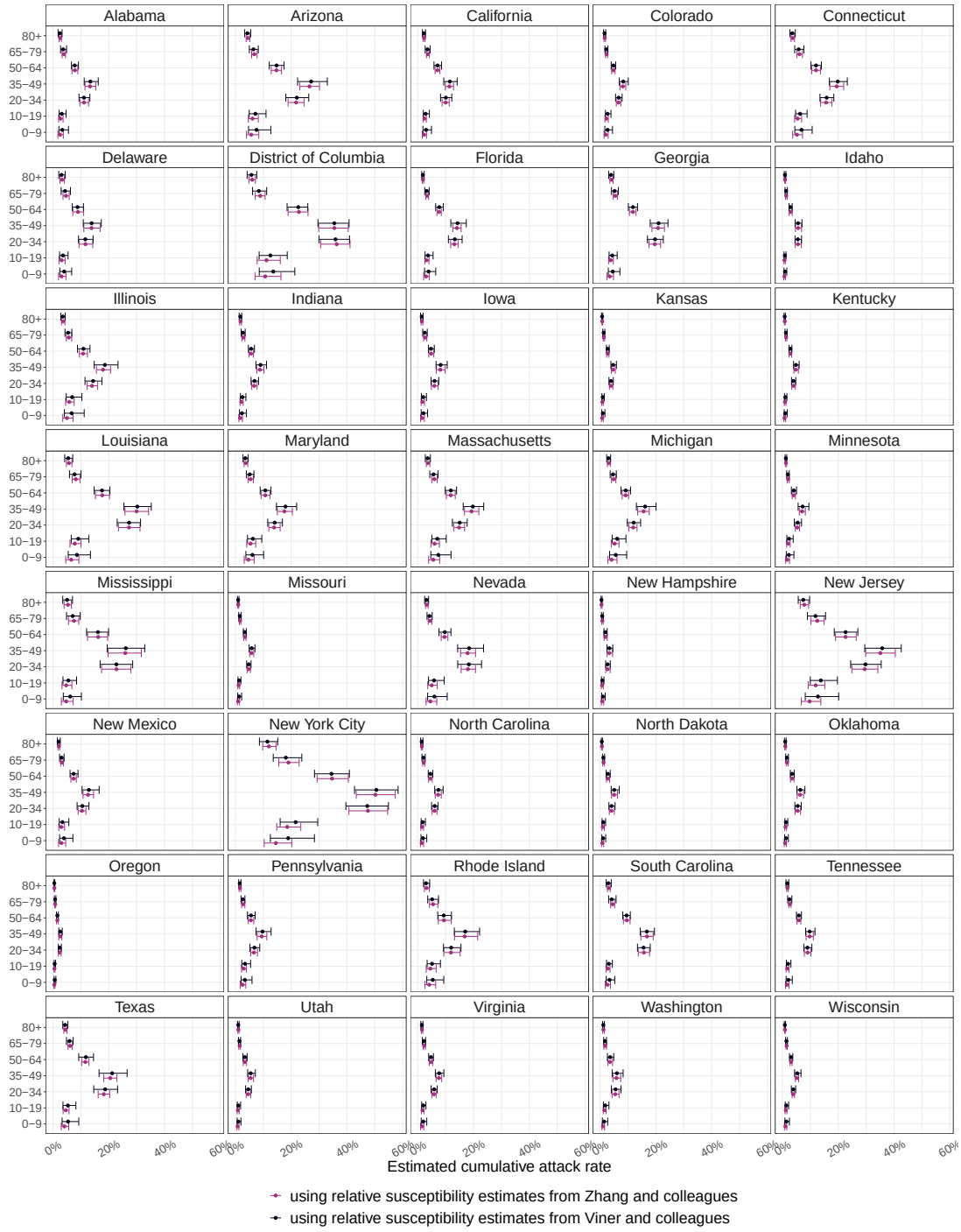

Figure S41: Age-specific cumulative attack rate estimates under the central model and under the alternative model that uses relative susceptibility estimates of Viner et al. [90]. Central model is in purple and alternative model is in black. Dots and error bars indicate posterior median estimates and 95% credible intervals of cumulated attack rates as of August 23, 2020.

References

1. Waksman, A., "Phones, Lambdas and the Joy of Snap-to-Place Technology", Available at https://enterprise.foursquare.com/intersections/article/phones-lambdas-and-the-joy-of-snap-to-place-techn/, (2018).
2. Foursquare Inc., "Pilgrim SDK", Available at https://enterprise.foursquare.com/products/pilgrim, (2020).
3. Dong, E, Du, H, Gardner, L, An interactive web-based dashboard to track COVID-19 in real time. *The Lancet Infectious diseases* **20**, 1473–3099, DOI 10.1016/S1473-3099(20)30120-1 (2020).
4. New York City Department of Health, "Coronavirus data", Available at https://github.com/nychealth/coronavirus-data/blob/master/totals/by-age.csv, (2020).
5. Levin, A. T. *et al.*, Assessing the Age Specificity of Infection Fatality Rates for COVID-19: Systematic Review, Meta-Analysis, and Public Policy Implications, Version 7. *medRxiv*, DOI 10.1101/2020.07.23.20160895 (2020).
6. Imperial College London COVID-19 Response Team, "COVID-19 Age specific Mortality Data Repository", Available at https://github.com/ImperialCollegeLondon/US-covid19-agespecific-mortality-data, 2020.
7. Alabama Public Health, "Demographics on Deaths", Available at https://alpublichealth.maps.arcgis.com/home/index.html, (2020).
8. Alaska Department of Health and Social Services Coronavirus Response, "Demographic Distribution of Confirmed Cases", Available at https://coronavirus-response-alaska-dhss.hub.arcgis.com/datasets/summary-tables, (2020).
9. Arizona Department of Health Services, "COVID-19 Deaths", Available at https://www.azdhs.gov/preparedness/epidemiology-disease-control/infectious-disease-epidemiology/covid-19/dashboards/index.php, (2020).
10. California Department of Public Health, "Statewide Case Statistics", Available at https://public.tableau.com/views/COVID-19CasesDashboard_15931020425010/Cases?:embed=y&:showVizHome=no, (2020).
11. Colorado Department of Public Health & Environment, "DPHE COVID19 State-Level Open Data Repository", Available at https://covid19.colorado.gov/data, (2020).
12. Connecticut Open Data, "COVID-19 Cases and Deaths by Age Group", Available at https://data.ct.gov/Health-and-Human-Services/COVID-19-Cases-and-Deaths-by-Age-Group/ypz6-8qyf, (2020).
13. Delaware Environmental Public Health Tracking Network, "Demographic Breakdown of Deaths", Available at https://myhealthycommunity.dhss.delaware.gov/locations/state, (2020).

14. Government of the District of Columbia, “Coronavirus Data”, Available at https://coronavirus.dc.gov/page/coronavirus-data, (2020).
15. Florida Division of Emergency Management, “Coronavirus: characteristics of Florida resident cases”, Available at https://www.floridadisaster.org/covid19/covid-19-data-reports/, (2020).
16. Georgia Department of Public Health, “Deaths in Georgia”, Available at https://dph.georgia.gov/covid-19-daily-status-report, (2020).
17. State of Hawaii – Department of Health, “What are the Ages, Gender, and Outcomes of COVID-19 Cases?”, Available at https://health.hawaii.gov/coronavirusdisease2019/what-you-should-know/current-situation-in-hawaii/, (2020).
18. Idaho Division of Public Health, “COVID-19 Demographics”, Available at https://coronavirus.idaho.gov/, (2020).
19. Illinois Department of Public Health, “Age Demographics”, Available at https://www.dph.illinois.gov/covid19/covid19-statistics, (2020).
20. Indiana State Department of Health, “Statewide Demographics for Deaths”, Available at https://www.coronavirus.in.gov/, (2020).
21. Iowa Department of Public Health, “Deaths by Age Group”, Available at https://coronavirus.iowa.gov/pages/outcome-analysis-deaths, (2020).
22. Kansas Department of Health and Environment, “Death summary”, Available at https://www.coronavirus.kdheks.gov/160/COVID-19-in-Kansas, (2020).
23. Kentucky Department for Public Health, “Deaths by Age Group”, Available at https://govstatus.egov.com/kycovid19, (2020).
24. Louisiana Department of Health, “Cases and Deaths by Age”, Available at https://ldh.la.gov/Coronavirus/, (2020).
25. Maine Center for Disease Control & Prevention, “Maine COVID-19 summary”, Available at https://www.maine.gov/dhhs/mecdc/infectious-disease/epi/airborne/coronavirus/data.shtml, (2020).
26. Maryland Department of Health, “Cases and Deaths Data Breakdown by Age Range and Gender”, Available at https://coronavirus.maryland.gov/, (2020).
27. Massachusetts Department of Public Health, “Deaths and Death Rate by Age Group”, Available at https://www.mass.gov/info-details/archive-of-covid-19-cases-in-massachusetts, (2020).
28. Michigan Department of Health and Human Services, “Deaths by Demographic Characteristics”, Available at https://www.michigan.gov/coronavirus/0,9753,7-406-98163_98173---,00.html, (2020).
29. Michigan Department of Health and Human Services, “Data requested to the Department of Health and Human Services”, Available at https://github.com/ImperialCollegeLondon/US-covid19-agespecific-mortality-data/blob/master/data/req/michigan%20weekly.csv, (2020).

30. Minnesota Department of Health, “Age group data table”, Available at https://www.health.state.mn.us/diseases/coronavirus/stats/index.html, (2020).

31. Mississippi State Department of Health, “COVID-19 Cases and Deaths by Age Group”, Available at https://msdh.ms.gov/msdhsite/_static/14,0,420.html, (2020).

32. Missouri Department of Health and Senior Services, “Deaths by Age Range”, Available at https://showmestrong.mo.gov/data/public-health/, (2020).

33. State of Nevada Department of Health and Human Services, “Results Filter For Demographics”, Available at https://covid19.ncdhhs.gov/dashboard, (2020).

34. New Hampshire Department of Health and Human Services, “Laboratory-confirmed COVID-19 cases”, Available at https://www.nh.gov/covid19/, (2020).

35. New Jersey Department of Health, “Deaths by Age Group”, Available at https://www.nj.gov/health/cd/topics/covid2019_dashboard.shtml, (2020).

36. New Mexico Department of Health, “Updated New Mexico COVID-19 cases”, Available at https://cv.nmhealth.org/newsroom/, (2020).

37. New York City Department of Health, “NYC COVID-19 Deaths Among Confirmed Cases”, Available at https://www1.nyc.gov/site/doh/covid/covid-19-data-archive.page, (2020).

38. North Carolina Department of Health and Human Services, “Demographic Data”, Available at https://covid19.ncdhhs.gov/dashboard, (2020).

39. North Dakota Department of Health, “Cases by Age Group”, Available at https://www.health.nd.gov/diseases-conditions/coronavirus/north-dakota-coronavirus-cases, (2020).

40. Oklahoma State Department of Health, “Total Deaths by Age Group”, Available at https://looker-dashboards.ok.gov/embed/dashboards/76, (2020).

41. Oregon Health Authority COVID-19, “Oregon’s COVID-19 Cases by Demographic Group”, Available at https://www.oregon.gov/oha/ph/datastatistics/pages/index.aspx, (2020).

42. Pennsylvania State Department of Health, “Age Distribution of Deaths”, Available at https://www.health.pa.gov/topics/disease/coronavirus/Pages/Cases.aspx, (2020).

43. Rhode Island Department of Health, “COVID-19 Rhode Island Data”, Available at https://ri-department-of-health-covid-19-data-rihealth.hub.arcgis.com/, (2020).

44. South Carolina Department of Health and Environmental Control, “Reported COVID-19 Deaths By Age Group”, Available at https://scdhec.gov/covid19/south-carolina-county-level-data-covid-19, (2020).

45. Tennessee Department of Health, “Case counts by 10-year age groups by day for all of Tennessee”, Available at https://www.tn.gov/health/cedep/ncov/data/downloadable-datasets.html, (2020).

46. Texas Department of State Health Services, "Age of Confirmed Fatalities", Available at https://dshs.texas.gov/coronavirus/TexasCOVID19CaseCountData.xlsx, (2020).

47. Utah Department of Health, "Total Deaths by Age", Available at https://coronavirus.utah.gov/case-counts/, (2020).

48. Vermont Department of Health, "Vermont COVID-19 Deaths by Age Group", Available at https://www.healthvermont.gov/covid-19, (2020).

49. Virginia Department of Health, "Cumulative (total) number of COVID-19 cases, hospitalizations, and deaths for each health district in Virginia", Available at https://data.virginia.gov/Government/VDH-COVID-19-PublicUseDataset-Cases_By-Age-Group/uktn-mwig, (2020).

50. Washington State Department of Health, "Deaths by Age Group", Available at https://www.doh.wa.gov/Emergencies/NovelCoronavirusOutbreak2020COVID19/DataDashboard, (2020).

51. Wisconsin Department of Health Services, "COVID-19 Historical Data by State", Available at https://data.dhsgis.wi.gov/datasets/covid-19-historical-data-by-state/data?orderBy=GEOID, (2020).

52. Wyoming Department of Health, "COVID-19 Map and Statistics", Available at https://health.wyo.gov/publichealth/infectious-disease-epidemiology-unit/disease/novel-coronavirus/covid-19-map-and-statistics/, (2020).

53. Davies, N. G. *et al.*, Effects of non-pharmaceutical interventions on COVID-19 cases, deaths, and demand for hospital services in the UK: a modelling study. *The Lancet Public Health* **5**, e375–e385, DOI 10.1016/s2468-2667(20)30133-x (2020).

54. Zhang, J. *et al.*, Changes in contact patterns shape the dynamics of the COVID-19 outbreak in China. *Science* **368**, 1481–1486, DOI 10.1126/science.abb8001 (2020).

55. Bi, Q. *et al.*, Epidemiology and transmission of COVID-19 in 391 cases and 1286 of their close contacts in Shenzhen, China: a retrospective cohort study. *The Lancet Infectious Diseases* **20**, 911–919, DOI 10.1016/s1473-3099(20)30287-5 (2020).

56. Flaxman, S., Mishra, S., Gandy, A., *et al.*, Estimating the effects of non-pharmaceutical interventions on COVID-19 in Europe. *Nature* **584**, 1–8, DOI https://doi.org/10.1038/s41586-020-2405-7 (2020).

57. Waterfield, T. *et al.*, Seroprevalence of SARS-CoV-2 antibodies in children: a prospective multicentre cohort study. *Archives of Disease in Childhood*, DOI 10.1136/archdischild-2020-320558 (2020).

58. Hoang, T. *et al.*, A Systematic Review of Social Contact Surveys to Inform Transmission Models of Close-contact Infections. *Epidemiology* **30**, 723–736, DOI 10.1097/ede.0000000000001047 (2019).

59. Potter, G. E., Handcock, M. S., Longini, I. M., Halloran, M. E., Estimating within-school contact networks to understand influenza transmission. *The Annals of Applied Statistics* **6**, 1–26, DOI 10.1214/11-aoas505 (2012).

60. Smieszek, T. *et al.*, How should social mixing be measured: comparing web-based survey and sensor-based methods. *BMC Infectious Diseases* **14**, 136, DOI 10.1186/1471-2334-14-136 (2014).

61. Aiello, A. E. *et al.*, Design and methods of a social network isolation study for reducing respiratory infection transmission: The eX-FLU cluster randomized trial. *Epidemics* **15**, 38–55, DOI 10.1016/j.epidem.2016.01.001 (2016).

62. Mossong, J. *et al.*, Social Contacts and Mixing Patterns Relevant to the Spread of Infectious Diseases. *PLOS Medicine* **5**, 1–1, DOI 10.1371/journal.pmed.0050074 (2008).

63. Prem, K. *et al.*, Projecting contact matrices in 177 geographical regions: an update and comparison with empirical data for the COVID-19 era. *medrXiv*, DOI 10.1101/2020.07.22.20159772 (2020).

64. Mistry, D. *et al.*, Inferring high-resolution human mixing patterns for disease modeling. *arXiv*, DOI 2020arXiv200301214M (2020).

65. Van de Kassteele, J., van Eijkeren, J., Wallinga, J., Efficient estimation of age-specific social contact rates between men and women. *Ann. Appl. Stat.* **11**, 320–339, DOI 10.1214/16-AOAS1006 (2017).

66. Van de Kassteele, J., "Contact-patterns", Available at https://github.com/kassteele/Contact-patterns, (2017).

67. IHME COVID-19 Forecasting Team, Reiner, R.C, Barber, R.M. *et al.*, Modeling COVID-19 scenarios for the United States. *Nature Medicine*, DOI https://doi.org/10.1038/s41591-020-1132-9 (2020).

68. Nouvellet, P, Bhatia, S, Cori, A, *et al.*, Report 26 - Reduction in mobility and COVID-19 transmission. *Imperial College London COVID-19 reports*, DOI https://doi.org/10.25561/79643 (2020).

69. Fisher, K. A., Tenforde, M. W., Feldstein, L. R., Lindsell, C. J., Shapiro, N. I., *et al.*, Community and Close Contact Exposures Associated with COVID-19 Among Symptomatic Adults $\geq$18 Years in 11 Outpatient Health Care Facilities — United States, July 2020. *MMWR. Morbidity and Mortality Weekly Report* **69**, 1258–1264, DOI 10.15585/mmwr.mm6936a5 (2020).

70. YouGov PLC., "Personal measures taken to avoid COVID-19", Available at https://today.yougov.com/topics/international/articles-reports/2020/03/17/personal-measures-taken-avoid-covid-19, (2020).

71. Hale, T. *et al.*, Variation in US states' responses to COVID-19. *Blavatnik School of Government*, Available at www.bsg.ox.ac.uk/covidtracker (2020).

72. Education Week, "Map: Coronavirus and School Closures", Available at https://www.edweek.org/ew/section/multimedia/map-coronavirus-and-school-closures.html, (2020).

73. Jarvis, C. I. *et al.*, Quantifying the impact of physical distance measures on the transmission of COVID-19 in the UK. *BMC Medicine* **18**, 124, DOI https://doi.org/10.1186/s12916-020-01597-8 (2020).

74. National Centre for Education Statistics, "Common Core of Data America's School database", Available at https://nces.ed.gov/ccd/, (2020).

75. Liu, Y, Gayle, A, Wilder-Smith, A, Rocklöv, J, The reproductive number of COVID-19 is higher compared to SARS coronavirus. *Journal of Travel Medicine* **22**, DOI 10.1093/jtm/taaa021 (2020).

76. Wutzler, T., lognorm: Functions for the Lognormal Distribution. R package version 0.1.6 (2019).

77. Ferguson, N *et al.*, Report 9: Impact of non-pharmaceutical interventions (NPIs) to reduce COVID19 mortality and healthcare demand. *Imperial College London COVID-19 reports*, DOI https://doi.org/10.25561/77482 (2020).

78. Verity, R *et al.*, Estimates of the severity of COVID-19 disease. *Lancet Infect Dis* **20**, 669–677, DOI https://doi.org/10.1101/2020.03.09.20033357 (2020).

79. Havers, F. P. *et al.*, Seroprevalence of Antibodies to SARS-CoV-2 in 10 Sites in the United States, March 23-May 12, 2020. *JAMA Internal Medicine*, DOI 10.1001/jamainternmed.2020.4130 (2020).

80. Carpenter, B *et al.*, Stan: A Probabilistic Programming Language. *Journal of Statistical Software* **76**, 1–32, DOI 10.18637/jss.v076.i01 (2017).

81. Cori, A., Ferguson, N. M., Fraser, C., Cauchemez, S., A new framework and software to estimate time-varying reproduction numbers during epidemics. *American journal of epidemiology* **178**, 1505–1512, DOI https://doi.org/10.1093/aje/kwt133 (2013).

82. Feehan, D. M., Mahmud, A., Quantifying population contact patterns in the United States during the COVID-19 pandemic. *medrXiv*, DOI https://doi.org/10.1101/2020.04.13.20064014 (2020).

83. Rosenberg, E. S. *et al.*, Cumulative incidence and diagnosis of SARS-CoV-2 infection in New York. *Annals of Epidemiology* **48**, 23–29, DOI 10.1016/j.annepidem.2020.06.004 (2020).

84. Centers for Disease Control and Prevention, "Commercial laboratory seroprevalence survey data", Available at https://www.cdc.gov/coronavirus/2019-ncov/cases-updates/commercial-lab-surveys.html, (2020).

85. McAloon, C. G. *et al.*, The incubation period of COVID-19: A rapid systematic review and meta-analysis of observational research. *medRxiv*, DOI 10.1101/2020.04.24.20073957 (2020).

86. Guo, L. *et al.*, Profiling early humoral response to diagnose novel coronavirus disease (COVID-19). *Clinical Infectious Diseases* **71**, 778—785, DOI https://doi.org/10.1093/cid/ciaa310 (2020).

87. Zhao, J. *et al.*, Antibody responses to SARS-CoV-2 in patients of novel coronavirus disease 2019. *Clinical Infectious Diseases* **71**, 2027—2034, DOI https://doi.org/10.1093/cid/ciaa344 (2020).

88. Pei, S., Kandula, S., Shaman, J., Differential effects of intervention timing on COVID-19 spread in the United States. *Science Advances*, DOI 10.1126/sciadv.abd6370 (2020).

89. Levin, A. T. *et al.*, Assessing the Age Specificity of Infection Fatality Rates for COVID-19: Systematic Review, Meta-Analysis, and Public Policy Implications, Version 5. *medRxiv*, DOI 10.1101/2020.07.23.20160895 (2020).

90. Viner, R. M. *et al.*, Susceptibility to SARS-CoV-2 infection among children and adolescents compared with adults: a systematic review and meta-analysis. *JAMA pediatrics*, DOI 10.1001/jamapediatrics.2020.4573 (2020).

91. Goldstein, E., Lipsitch, M., Cevik, M., On the effect of age on the transmission of SARS-CoV-2 in households, schools and the community. *medRxiv*, DOI 10.1101/2020.07.19.20157362 (2020).